https://doi.org/10.5194/egusphere-2026-2106
Preprint. Discussion started: 4 June 2026

An experiment to resolve system-scale lake ice properties shaped by environmental processes

Felix Strobel[1], Gregor Hillers[1], Tom Jilbert[2], John Loehr[3], Christian Stranne[4], Tahvo Oksanen[1], Jonathan Vänskä[1], Roméo Courbis[1], Annukka Rintamäki[1], Amir Sadeghi-Bagherabadi[1], Lasse Weißgräber[5], Yinshuai Ding[1], Marc de Langenhagen[6], Eduardo Valero Cano[1], Kwabena Atobra[1], Vicent Doñate Felip[4], Valtteri Hopiavuori[1], Max Kankainen[2], Mohammad Alem Khodadadi[1], Kauri Kolehmainen[1], Emma Makkonen[1], Liisa Nygrén[1], Eero Purhonen[1], Niklas Rolleberg[7], Jasmiina Tuomiranta[1], Tommi Vuorinen[1], Aurélien Mordret[8], Cédric Schmelzbach[9], Ludovic Moreau[10], Olivier Coutant[10], and Céline Hadziioannou[5]

[1]Institute of Seismology, University of Helsinki, Helsinki, Finland
[2]Department of Geosciences and Geography, University of Helsinki, Helsinki, Finland
[3]Lammi Biological Station, University of Helsinki, Helsinki, Finland
[4]Department of Geological Sciences, Stockholm University, Stockholm, Sweden
[5]Institute of Geophysics, University of Hamburg, Hamburg, Germany
[6]Belle Etoile Production, Chambéry, France
[7]Department of Engineering Mechanics, KTH Royal Institute of Technology, Stockholm, Sweden
[8]Geological Survey of Denmark and Greenland, Copenhagen, Denmark
[9]Institute of Geophysics, ETH Zürich, Zürich, Switzerland
[10]Institut des Sciences de la Terre, University Grenoble Alpes, Grenoble, France

Correspondence: Felix Strobel (felix.strobel@helsinki.fi)

Abstract. The multi-scale composition, structure, and dynamics of seasonal ice floating on freshwater lakes are influenced by ambient conditions. Here we describe a comprehensive geoscience experiment for lake system imaging and monitoring of spatiotemporal ice property variations. We explore the resolution of meteorological and environmental driving mechanisms that can include the quantification of methane degassing from boreal lakes. The project centerpiece is a seismic array of 210 geophones arranged in an aperiodic tiling configuration that was deployed in February 2025 on the ∼25 cm thick ice of Lake Pääjärvi in southern Finland. The 10-km scale lake array is complemented by three dense circular arrays, 31 land-based sensors, eight broadband seismometers, three accelerometers, a rotational seismometer, a Distributed Acoustic Sensing system with a 1 km-long fibre optic cable, an underwater echosounder, a microphone, a Ground Penetrating Radar (GPR) survey, water chemistry measurements, manual ice thickness sampling and ice coring, and meteorological observations. We observe the strongly dispersive QS flexural mode and the weakly or non-dispersive QS_0 and HS_0 modes excited by hammer shots, icequakes, and environmental sources and reconstruct the average propagation using beamforming and noise correlations. Propagation speed estimates for the three modes range approximately between 20–100 m s^{-1}, 3000–3400 m s^{-1}, and 1650–1800 m s^{-1}, respectively. High values for the Poisson's ratio $\nu = 0.42$ and Young's modulus $E = 8.59$ GPa reflect the overall competent characteristics of the ice referred to as teräsjää (steel ice). Seismic activity in the 0.03–0.2 Hz band increases during high wind speed episodes, and signals above 0.1 Hz correlate with rapid air-temperature cooling events. The GPR profile images

https://doi.org/10.5194/egusphere-2026-2106
Preprint. Discussion started: 4 June 2026

the spatial ice variability across the lake that is compatible with the in-situ measurements, and we show that seismo-acoustic observations can be inverted for similarly compatible thickness estimates. The geochemical water and ice sample analysis suggests Lake Pääjärvi is a source of methane, and localized ebullition can potentially be resolved from echosounder data. This synthesis demonstrates that the application of environmental seismology concepts can form a bridge between bottom-up ebullition monitoring and remote-sensing approaches.

1 Introduction

Seasonal ice and snow cover of high-latitude aquatic systems has a direct impact on Earth's radiative forcing through its role in the albedo feedback (Perovich and Polashenski, 2012) and on carbon cycling through controlling the length of the biological growth season (Arrigo et al., 2008). Ice cover in subarctic lakes and the Arctic Ocean therefore constitutes an essential component of the climate system (Barry et al., 1993; Brown and Duguay, 2010), but climate change is altering the spatio-temporal dynamics of winter ice cover. Both ice thickness and the duration of ice cover are in decline over recent decades (Singarayer et al., 2006). The integrity of the affected winter ice is important for shoreline communities using ice cover for transport, fisheries, and recreational activities, and for species in high-latitude ecosystems whose habitats depend upon ice cover (Vincent et al., 2011; Griffiths et al., 2017). It is thus important to develop geophysical methods that are calibrated by in-situ observations for fast, high-resolution, and accurate estimates of ice properties and ice dynamics.

The ice density, thickness, and intrinsic elastic properties are controlled by the microscale and macroscale composition and structure. Seasonal ice formation ensues during the freezing of surface waters in winter, and proceeds through a complex sequence of snowfall, compaction, melting, and refreezing (Michel and Ramseier, 1971). These processes generate a layering of the seasonal ice cover, characterized by primary and congelation ice underlying layers of so-called superimposed ice derived from recrystallized snowmelt and flood waters (Leppäranta, 2023). Spatial variability in surface water temperatures, and the accumulation of snow, can significantly alter the structure and physical properties of ice (Leppäranta, 2010). At larger scales, ice layers are subject to continuous forcing from the surrounding environment, including changes in temperature, wind stress, and exposure to advective processes such as currents and riverine inputs that can in turn affect the structure of the ice.

Warming of the high northern latitudes is expected to accelerate the natural production of methane (CH_4) due to enhanced rates of microbial activity in organic-rich soils and sediments. Methane is the second most important greenhouse gas, responsible for approximately 20% of the overall increased atmospheric radiative forcing observed since 1750 (Stocker et al., 2013). In aquatic systems, enhanced methane production may be expressed as ebullition of methane gas from sediments and the occurrence of bubble trains in the water column (Rosentreter et al., 2021). Recent studies have demonstrated that bubble inclusions of methane gas in lake ice can be detected and possibly quantified by remote sensing (Engram et al., 2020). However, multiple processes can control the inclusion of gas bubbles in ice. These include exsolution of dissolved air during formation of congelation ice (Leppäranta, 2010) and trapping of atmospheric gases in superimposed ice during refreezing of snowmelt and flood waters (Palosuo, 1965), leading to a wide range of bubble morphologies and gas compositions (Boereboom et al., 2012). These processes can also be modified by climate change, due to changes in the frequency of snowfall and snowmelt as well as

https://doi.org/10.5194/egusphere-2026-2106
Preprint. Discussion started: 4 June 2026

the thickness of the initially formed hard ice layer. The extent to which inclusion of gases from methane ebullition and other sources affect the physical properties of ice is uncertain. Moreover, understanding of how gas inclusions interact with other characteristics to determine overall integrity of the ice is poor.

In this data paper we describe a dense seismic array experiment to monitor and image a full-scale seasonal lake ice cover on the 10 km scale in southern Finland. Seismic methods analyze wave propagation in the cryosphere including glaciers, ice sheets, sea ice, lake and river ice, and the seasonally freezing ground. Icequake or frostquake signals and the ambient wavefield excited by external and internal sources carry information about the ice dynamics and can resolve space-time variations of the density, thickness, and elasticity reflecting its micro- and macrostructure. Seismic techniques can thus be an efficient sensing and imaging tool to characterize ice properties that are governed by environmental processes and the dynamics of frozen aquatic systems. We explore here the possibility to resolve spatially variable encapsulated gas using seismic tomography.

Our experiment was performed in February 2025 on Lake Pääjärvi, 100 km North of Helsinki. The data acquisition on the ∼25 cm thick ice layer is discussed in Section 2. The seismic deployment uses 340 geophones, 8 seismometers, 3 accelerometers, and a rotational sensor that are configured in a lake shore network, a monotile lake-scale array, and three small beamforming arrays. The experiment includes further a ∼1 km long fibre optic cable, a microphone, ground penetrating radar, an echosounder, manual ice thickness measurements, geochemical probing of the lake sediments, water column, and ice, and documentary filming. In Section 3 we show examples of wave propagation signals observed with the diverse instrumentation, the ice thickness and modulus estimates obtained with different seismic analysis techniques, and the hydroacoustic ebullition sounding and the geochemistry analysis results. In Section 4 we evaluate the consistency of the initial observations and results, the implications for resolving spatio-temporal variations of ice properties using tomography, and the significance for lake system scale environmental monitoring.

2 The experiment

2.1 The environment of Lake Pääjärvi

Lake Pääjärvi is located in southern Finland at 61°06′ N, 25°08′ E (Fig. 1). To facilitate fieldwork logistics, we used the adjacent University of Helsinki Lammi Biological Station which is located 200 m away from the the western bay of the lake. The ∼10 km scale allowed us to accomplish the deployment with a team of 16 with reasonable effort. The lake was formed following isolation from the Yoldia Sea at 10800 yr BP (Valpola and Ojala, 2006) after retreat of ice cover from the area at 11700 yr BP. The regional terrestrial landscape is greatly influenced by glacial till and moraine formations as well as fine-grained sediments (Ruuhijärvi, 1974). The underlying bedrock of the lake is primarily composed of granite and gneiss and the lake basin is influenced by two shear zones that transect the lake in approximately east-west and north-south directions. Motion along these shear zones formed a basin with significant relief. On a regional scale the lake is comparatively deep with a maximum depth of 87 m and a mean depth of 14.4 m (Ruuhijärvi, 1974).

The lake belongs to the Kokemäenjoki River catchment area with five major inlet streams located on the west and east ends of the lake and on the northern shore. Landcover classification in the 244 km^2 Lake Pääjärvi catchment area is governed by

https://doi.org/10.5194/egusphere-2026-2106
Preprint. Discussion started: 4 June 2026

coniferous forests (59%), agricultural land (15%), and peatlands (11%) (Arvola et al., 1996; Hakala et al., 2002), and the run-off influences the mesotrophic classification of the lake itself. The humic waters typically have a Secchi depth of 1.8 m (Arst et al., 2008). The Teuronjoki River drains the lake from the southern shore. Muddy gyttja sediments accumulate throughout the lake, with organic matter in the surface layers approximately 10% by mass as determined from loss on ignition (Valpola and Ojala, 2006). In hypoxic accumulation areas sediments may be laminated (Simola and Uimonen-Simola, 1983). Methane concentrations in excess of 500 μmol L^{-1} are observed in porewaters of the uppermost 10 cm of the sediment column (Rissanen et al., 2023), indicating a shallow methanogenesis zone, although active methaontrophy limits the flux of methane to the water column.

2.2 Meteorological conditions

We use meteorological data recorded at stations from the Finnish Meteorological Institute (FMI). The meteorological station Hämeenlinna Lammi Pappila is located at the Lammi research station. This station records air temperature, dew-point temperature, relative humidity, precipitation amount, and snow depth data in 10 minute intervals (Fig. A1). Figure 2a shows the temperatures between 1 October 2024 and 1 May 2025 in relation to the deployment period of the 31 stations around the lake between November 2024 and May 2025 and the main experiment in February and March 2025. Sub-zero temperatures start to become pervasive around the time of the lake shore deployment. The realization of the experiment was jeopardized by temperature fluctuations in December 2024 and January 2025 that inhibited the steady formation of a stable ice layer, but at least during the first half of the main deployment the temperatures reached -5°C and colder with a peak of -20°C (Fig. 2b). Some few centimeters deep drift snow patches formed during the first week of the main experiment. The mild temperatures in late February melted these patches and formed extensive puddles that evaporated or froze over.

We use observations of air pressure and wind speed and direction from the Hämeenlinna Katinen and Asikkala Pulkkilanharju stations that are located 35 km to the west and 30 km to the north-east, respectively. The wind speed varies between 0 and 10 m s^{-1}, and the records show different degrees of similarity at different times at the two distant sites (Fig. 2c). In February and early March the nighttime exceeds daytime duration, although daylight already accounts for a significant fraction of the day. On 10 February, apparent sunrise occurs at 06:15 UTC and sunset at 14:53 UTC or 08:15 and 16:53 local time, respectively. By 1 March, the length of the day has increased by 107 minutes, with sunrise at 05:20 UTC and sunset at 15:45 UTC.

2.3 The seismic deployment

The seismic experiment involved several instrument types to collect a diverse dataset of elastic wave propagation observations in the ice for cross-validating multiple monitoring and imaging analyses based on ballistic and scattered or reverberating waves. We used 340 geophones, 8 broadband seismometers, 3 accelerometers, a distributed acoustic sensing (DAS) cable, and a rotational sensor. The lake shore array operated from 22 November 2024 to 24 April 2025. Most instruments on the frozen lake surface were deployed between early February and early March 2025. The main lake ice array was deployed between 10–13 February and 2–3 March 2025. Installation and recovery were accomplished by small teams. Up to 16 people roamed

https://doi.org/10.5194/egusphere-2026-2106
Preprint. Discussion started: 4 June 2026

the ice at the same time. During the three weeks of the active deployment one person (F.S.) performed daily maintenance tasks including system health checks, battery swapping, sensor leveling, and operational activities including hammer shots and differential GPS (DGPS) measurements.

The FINNSIP instrument pool (Hillers et al., 2025) provided 340 Geospace large-N Land Cartesian 5 Hz GS-One LF geophones, each paired with a GSB-3 seismic recorder, 8 Güralp 3ESPC broadband seismometers with Güralp Minimus digitizers, 3 Güralp Fortis accelerometers with Güralp Minimus digitizers, and 12 V lead batteries for the Güralp instruments. We deployed a blueSeis-3A fiber optic gyro rotational seismometer and a DAS system composed of a FEBUS A1 interrogator and a 1,200 m fiber optic cable. Table 1 summarizes the dataset sizes obtained with the different instrument types. The total size is about 20 TiB.

Measurement Type	Data Volume
Geophones on ice	12.3 TiB
Geophones on land	2.3 TiB
Broadband seismometers	11.1 GiB
Accelerometers	7.9 GiB
Rotation sensor	3.8 GiB
DAS	3.7 TiB
Microphone	291 GiB
GPR survey	19 MiB
Audiovisual footage	220 GiB

Table 1. Data volumes of different measurement types

2.3.1 The 31-sensor lake shore network

31 geophones were deployed on land along the lake shore for 153 days (Fig. 3) for the analysis of wave propagation across the shore. External Li-ion batteries were used to extend the acquisition. The sampling rate was 500 Hz. The instruments were installed in the upper 50 cm of soil at a distance between tens of meters and several hundreds of meters from the lake shore. The largest distance to the shoreline is 550 m for a station in the northeast.

2.3.2 The 210-sensor monotile lake ice array

The main seismic array (Fig. 3) consists of 210 stations that are arranged in a geometry that is based on the Specter aperiodic tiling introduced by Smith et al. (2024a, b). This unique monotile configuration is optimal for detection and seismic imaging, including plane-wave beamforming and ambient noise tomography applications (Mordret and Grushin, 2025). The Specter design makes the seismic array very robust to spatial aliasing, and the pattern ensures a smooth and continuous distribution of inter-station distances and avoids sampling gaps and redundancy common in periodic arrays. The array design yields a quasi-homogeneous azimuthal coverage of station pairs, however, the elongated shape of lake results in a directional sensitivity of

https://doi.org/10.5194/egusphere-2026-2106
Preprint. Discussion started: 4 June 2026

the array. The Lake Pääjärvi array has been designed using the Jupyter Notebook tools of Mordret and Grushin (2025), which require the definition of a closed boundary polygon and the number of stations inside the polygon. We use a buffer zone of 100 m to the lake shore and island contours to avoid the deployment on potentially thin ice.

A one to two meters wide N-S trending rift zone located 4 km east of the western end of the lake extends between the northern and southern shoreline (Figs. 1, 4g). Safety concerns prevented the installation of two geophones in its vicinity. This and the irregular lake shape and the islands break the monotile pattern. Associated gaps were mitigated by the manual deployment of twelve additional stations. These are the red indicated geophones in Figure 3 that are not connected to the monotile pattern. The minimum and median nearest neighbors interstation distances are 165 m and 188 m, respectively. The median deviation between the designed positions and the location estimates is 2.145 m. The locations were estimated with an RTK DGPS system.

Teams of two to four installed the lake ice geophones between 9 and 13 February 2025 following a consistent procedure. At each ice station two 15 cm wide auger holes were drilled. The first 10 cm deep hole held the geophone, and the second hole immediately south pierced the ice. This hole was used for the ice thickness measurement and provided enough space to organize the cable between the geophone and the GSB logger. The geophone is oriented to geographical north (Fig. 4b), and drill powder and water were mixed to fill the holes with freezing slush that led to the good coupling of the sensors and supported a marker stick (Fig. 4a). The sampling rate for all geophones deployed on the ice was 2,000 Hz.

The instruments were recovered on 3 and 4 February 2025. At each site, the geophone location was determined with DGPS. We measured the in-situ ice thickness again through auger holes. The geophone orientation was again measured relative to geographic north and a photograph of the bubble level was taken to document the final alignment. The geophones tended to tilt south in response to the differential melting induced by the black logger cable.

For the planning, deployment, maintenance, retrieval, and analysis of geospatial data the QGIS software with the QField plugin and the QField phone application were used (QGIS Development Team, 2009). The locations of the monotile array stations and the circular array locations (Sec. 2.3.3) were planned in QGIS and then synchronized to the QField phone applications for navigation using the QField cloud service. A database was implemented for logbook entries for each sensor. Station documentation including photo and screenshot attachments was constantly updated. The daily synchronization of the documentation facilitated the management and trouble shooting.

2.3.3 The three circular lake ice arrays

Three circular arrays were installed in the central part of the lake (Fig. 3) to facilitate beamforming and the computation of gradients for array-derived rotational (ADR) motion estimates. They consisted of concentric rings with equally spaced sensors. At the center of each array we placed a broadband seismometer and an accelerometer on the same concrete slab and a geophone in the ice. The central Array A (Fig. 4c) is equipped with the rotation sensor that is put on the same concrete slab to compare ADR estimates to instrumental records of rotational motion. At all arrays, the first ring with a radius of 2 m consist of five instruments, followed by seven instruments at 4.3 m, and nine instruments at 9.25 m distance. Array A had a fourth ring with eleven instruments at a radius of 20 m. The first ring of Array A has broadband sensors, other ring sensors are geophones.

https://doi.org/10.5194/egusphere-2026-2106
Preprint. Discussion started: 4 June 2026

For the Güralp 3ESPC seismometers the sampling rate was set to 250 Hz and the recenter threshold to 6 V. The power was provided by 12 V/70 Ah lead batteries which had to be swapped and recharged once during the deployment. Each seismometer was installed on a concrete slab for stability. The instrument was covered with an inverted bin and a stone brick on top. The bucket rim was placed on the ice and did not touch the concrete slab. The data logger and battery were placed in a plastic box next to the bin.

The three Güralp Fortis accelerometers were installed at the centers of the arrays and used the same data logger model and power supply configuration as the seismometers. The sampling rate was 500 Hz and the gain was 0.51 g. We relied on a RaspberryPi running SeisComp for the data acquisition of the blueSeis-3A rotation sensor in Array A. The power was supplied by six 12 V/70 Ah lead batteries from the FINNSIP instrument pool and had to be swapped and recharged every two to three days. The sampling rate was 200 Hz. An aluminum box with a cut out floor was placed over the seismometer, accelerometer, and rotational motion instruments for protection (Fig. 4d). With the onset of thawing temperatures on 22 February 2025 the concrete slabs tilted and required regular leveling of the sensors. All instruments on the large concrete slab were repositioned and reoriented after one week in response to tilting.

2.3.4 The 26-sensor lake ice line array

A line array of 26 geophones was deployed along the first DAS segment at a distance of approximately 20 cm from the cable to provide reference observations for calibration (Fig. 3). The spacing of four meters results in a 100 m array length.

2.3.5 The Distributed Acoustic Sensing DAS unit

Our DAS system consisted of a FEBUS A1 interrogator and a 1,200 m long fiber optic cable. The first 36 m and last 164 m of the cable were rolled to remove coherent background noise, resulting in a 1,000 m long active cable. The interrogator installation on the western lake shore of the central lake part (Fig. 3) was facilitated by power supply on private property. From this location, the fiber-optic cable extended onto the lake in three segments. The orientation of the first 400 m long segment was N90°E, and the orientations of the second and third 300 m long segments were N135°E and N180°E, respectively. The cable was rolled out on the ice surface without further efforts to improve the coupling (Fig. 4f). For stability, every few tens of meters and at the corners the cable was fixed by freezing slush ice. The DAS system recorded nanostrain-rate at a sampling rate of 2,500 Hz with a 10 m gauge length from 13 to 26 February 2025. The channel spacing was first set to 9.6 m and reduced to 2 m after seven days, but the gauge length remained at 10 m.

2.3.6 Hammer shots

Between 26 February 2025 and 1 March 2025 time triggered hammer shots were applied at 49 locations along five lines and a circle on the ice (Fig. A2). At all locations at least five vertical hammer shots were applied. At each of the twelve locations around the central array at least five additional hammer shots were applied in the clockwise transversal direction. For this, a steel H-beam was placed on the ice and laterally excited. The positions were estimated with a handheld GPS device.

https://doi.org/10.5194/egusphere-2026-2106
Preprint. Discussion started: 4 June 2026

2.4 Acoustic monitoring

The vertical component motion of wave modes propagating in a floating ice sheet or slab at a phase velocity that is higher or equal to the velocity of sound in air can couple from the ice to the atmosphere. The radiated acoustic energy in the audible frequency range can cause a phenomenon that is popularly referred to as singing ice. These seismo-acoustic signals can be detected with microphones installed above the ice (Press et al., 1950; Schmelzbach et al., 2022; Wetter et al., 2023; Romeyn and Hanssen, 2023; Schmelzbach et al., 2025). The frequency, duration, and amplitude of air-coupled waves are controlled by the ice properties. To complement the seismic acquisition we deployed an acoustic sensor consisting of four microphones arranged in a 6 cm square configuration controlled by a RaspberryPi mini-computer (Wetter et al., 2023; Schmelzbach et al., 2025). The sensor was located on the ice, about 10 m away from the shore (Fig. 3) and at 2 m distance from the DAS cable, on a tripod at 110 cm above the ice surface (Fig. 4e). The sensor operated continuously from 18 February 2025 to 4 March 2025 and recorded acoustic signals in the 20 Hz to 4 kHz range. Timing accuracy was controlled by regularly synchronizing the internal clock with the Pulse-Per-Second pulse recorded with a GNSS receiver to full-second accuracy. For reference, we installed a geophone below the microphone from 26 February 2025 to 4 March 2025.

2.5 Ground Penetrating Radar survey

Ground Penetrating Radar (GPR) is a suitable near-surface geophysics tool that uses propagation and reflection properties of electromagnetic waves to image the layered shallow subsurface structure. It can provide accurate snow cover and ice thickness (Meng et al., 2025) estimates to complement the in-situ measurements and tomography results (Matsumoto et al., 2019; Moreau et al., 2020; Xing et al., 2022). We used a Zond-12 GPR system with a 900 MHz antenna to collect GPR data approximately along the longitudinal axis of the lake (Fig. 5). The acquisition system was mounted on a fiberglass sledge, which was towed by an all terrain vehicle at a speed of 5 km h^{-1}. The survey line length was 9.98 km and the data acquisition was completed in approximately 2 hours. Due to changing weather conditions the data acquisition was completed in five individual time periods over two days, on 8 and 9 February 2025. The obtained dataset includes five segments (Fig. 5) and has 13,796 traces, and each trace is recorded over 50 ns at a sampling rate of 10.24 GHz. The complete GPR dataset in SEG-Y format has a file size of 19 MiB.

2.6 Hydroacoustic sounding

It is challenging to collect ground truth gas ebullition data to provide reference observations for an ice tomography. We deployed a state-of-the-art autonomous wideband echosounder on the ice to directly monitor ebullition during the field campaign. This is considered to be a reliable method for estimating gas flux and has been used in a wide range of settings (Weidner et al., 2019; Li et al., 2020). The acoustic footprint of the echosounder is on the order of meters, hence observations are limited to local ebullition at a specific spot in the lake. This emphasizes the challenge of estimating lake ebullition with traditional methods, but is intended be used here for comparison with the local ice properties and later estimates from a tomography at the corresponding location.

https://doi.org/10.5194/egusphere-2026-2106
Preprint. Discussion started: 4 June 2026

The acoustic midwater system consisted of a Simrad WBT Tube operating two ES38-18DK wideband split-beam transducers in sequential ping mode (Fig. 6a, b). The WBT was connected to a local laptop. The system was controlled and monitored remotely via a 4G modem (Fig. 6a). Power was supplied by six 12.8 V, 180 Ah $LiFePO_4$ batteries for the duration of the deployment. Both transducers were calibrated on site with a Ø38 mm tungsten sphere using standard procedure (Foote et al., 1987; Demer et al., 2015). Three deployments were accomplished during 10 February 2025 to 14 February 2025 and lasted around one day each (Table 2). The first, ICE1, probes the deepest part of the lake, and ICE2 and ICE3 are located south and east of inlet streams, respectively.

Station	Position (Lat, Lon)	Duration (UTC)	Bottom depth (m)
ICE1	61.056870°N, 25.126431°E	2025-02-10 13:17 – 2025-02-11 08:06	80
ICE2	61.070457°N, 25.131033°E	2025-02-11 09:57 – 2025-02-12 08:59	60
ICE3	61.050846°N, 25.060490°E	2025-02-12 10:50 – 2025-02-14 12:04	14

Table 2. Parameters of the hydroacoustic sounding deployments. Locations are indicated in Figure 6d. Position precision is on the decimeter scale.

2.7 Environmental data acquisition

2.7.1 Ice thickness

The spatially variable ice thickness was measured during the geophone installation (Fig. 7a) and during the recovery of the instruments (Fig. 7b, Section 2.3), and during the geochemical sampling (Section 2.7.2). Thickness was measured through a drill hole using a ruler with a hook, which allows readings to ∼0.5 cm accuracy. The measurements during the deployment phase were completed in a five day long time window between 9 to 13 February 2025 (Fig. 7e). During the recovery of the instruments the measurements were completed within two days (Fig. 7f). Ice thickness measurements outside these time windows are not included in the discussion.

2.7.2 Environmental Geochemistry

During the main experiment we carried out sampling for environmental parameters at 56 locations divided into three groups based on the applied sampling protocol (Fig. 6d). At eight locations, we first retrieved an ice sample by drilling a triangle of adjacent holes with a 15 cm diameter ice-screw and extracting the central portion (approximate mass 5–10 kg). We then photographed the cross-sectional profile of the ice sample to determine visually the thickness of the two principal layers. Using a saw, we extracted subsamples of approximately 100–250 g from the uppermost and lowermost 5 cm of the ice.

We retrieved water column samples from directly under the ice and at 5–10 m intervals throughout the water column using a Limnos bottle sampler. We further deployed a water quality sonde (YSI instruments) to determine dissolved oxygen, temperature, and pH at equivalent depths to the bottle samples. We then retrieved a sediment core using a HTH/Kajak gravity coring device with Perspex tube pre-drilled for porewater sampling. From the core, we collected porewaters using Rhizons.

https://doi.org/10.5194/egusphere-2026-2106
Preprint. Discussion started: 4 June 2026

We transfered both water column and porewater samples to plastic syringes pre-loaded with 0.1 M HNO_3 to ensure conversion of dissolved inorganic carbon to CO_2 (Jilbert et al., 2020). At the remaining 48 locations, we took only the ice samples as described above. From 29 randomly selected locations of the total 56 ice sampling locations, we determined bulk ice density for uppermost and lowermost 5 cm of the ice by volume displacement in a measuring cylinder, assuming a density of 0.917 g cm^{-3} for solid ice with no gas inclusions (Mellor, 1980). From these data, we estimated the theoretical volume of gas space in the ice samples.

We determined methane CH_4 and dissolved inorganic carbon concentrations in water and porewater samples by gas chromatography after headspace equilibration in the sampling syringes and transfer of headspace gas to Exetainer vials for storage. Additionally, we determined CH_4 in ice samples after melting and headspace equilibration in Tedlar bags. Concentrations in the dissolved phase were estimated using Henry's Law applying solubility coefficients for CH_4 and CO_2 from Wiesenburg and Guinasso (1979) and Weiss and Price (1980) respectively.

2.8 Documentary filmmaking

We collected audiovisual material of the environment and the deployment activities, and conducted interviews with each team member to make a 15 min long documentary for science communication, outreach, and education (https://youtu.be/KPWA8vkfZjc). The documentarist opted for lightweight technical equipment not exceeding 15 kg to support agility. We worked with a Sony A7s3 camera, two versatile lenses (24−70 mm f2.8 and 70−200 mm f4), and a 85 mm f1.8 fixed focal length lens for the interviews. We preferred a RONIN DJI electronic stabilizer over a shoulder mount and tripod to support the filming on slippery surfaces. A Mavic3 drone captured the wide aerial shots of the lake to help give a sense of scale, and we used a waterproof GoPro camera mounted to a stick for underwater images. The close-up photos of the ice and the aerial images of the ice texture support the conceptual integration of the observations obtained with the different analysis techniques. The audiovisual dataset is 220 GiB large but not included in the publicly available data repository because of personal rights constraints.

3 Data examples and initial observations

3.1 Ice thickness

The homogeneous sampling of the system-scale in-situ ice thickness provides essential ground truth observations for referencing and calibration. Measurements collected during the seismic instrument deployment yield values between 11 and 30 cm, with a mean of 20.7 cm (Fig. 7a, g). At the time of the geochemical sampling, we find that the thickness scales of the soft surficial ice layer and the hard basal ice layer are around 2 cm and 25 cm, respectively. During the instrument recovery, values ranged between 21 and 35 cm with a mean of 26.4 cm (Fig. 7b, h). The time between paired measurements at the same site ranged from 19 to 22 days and revealed a thickness increase ranging from 1 to 10 cm with a mean of 5.6 cm (Figure 7c, h). This corresponds to a relative growth between 4% to 60%, with a mean increase of 28% (Fig. 7i). The spatial ice thickness

https://doi.org/10.5194/egusphere-2026-2106
Preprint. Discussion started: 4 June 2026

distribution is heterogeneous. At first the ice tends to be ∼5 cm thicker in the more narrow bays in the western and eastern parts of the lake (Fig. 7a). This spatial variability is persistent (Fig. 7b) but decreases during the duration of the experiment because the ice thickness difference and the growth ratio are larger in the central area (Fig. 7c, d). Potential variations across the rift zone (Fig. 1) are not resolved with the station location sampling.

3.2 Seismic data

3.2.1 Data availability and quality

After deinstallation the geophone data was downloaded from the GSB loggers. Records in the proprietary Geospace format were first converted to SEG-Y and then to MiniSEED using ObsPy tools (Beyreuther et al., 2010). With 98.7% (Strobel et al., 2026) the geophone data availability is very complete. The missing fraction is associated with data gaps at only three stations on land, lake ice, and on the Array A concrete slab.

The data return from the three accelerometers is also almost complete with 99.9%, except for the sensor in the center of Array B with its 15 short gaps of 11 to 120 s. The data return from the eight seismometers is 98.85%. The longest gaps associated with drained batteries are observed at two sensors for 19 February 2025 21:05 to 22 February 2025 09:16 (UTC) and for 20 February 2025 00:44 to 21 February 2025 14:48. Two stations have full records, and the remaining four seismometers yield records that contain only a few gaps of several seconds to a few minutes length. At one Array A station strong tilt yield a loss of ice motion observations between 13 February 2025 15:00 and 21 February 2025 15:00 since only recenter attempts of the sensor are recorded.

The rotation sensor has a major data gap between 16 February 2025 22:22 and 19 February2025 13:58 that we attribute to reception problems of the GNSS antenna. The records have a time difference of around 1.5 s compared the co-located seismometer before the gap but no time difference immediately after the manual restart. Several short overlaps of data as well as short gaps occurred when a new file is written at midnight. The overall data quality varies across the deployment period. The records contain significant amplitude spikes which are most likely artifacts from the sensor. The measurement principle of the rotation sensor (Schreiber et al., 2009; Rossi et al., 2025) yields constant time series offsets that are governed by the earth's rotation. However, the observed offset values differ from these predictions which implies the need for calibration.

3.2.2 Ice wave field signatures

Despite the repeated acquisition glitches of the rotational sensor, the obtained icequake waveforms shown in Figure 8a are consistent with the observations from the other three colocated sensor types that are all obtained at the central Array A. For comparison the geophone and seismometer data is differentiated. The three observations of vertical acceleration exhibit the theoretically predicted in-phase relationship with the transverse rotation rate (Igel et al., 2007). The vertical component records show the dispersive quasi-Scholte mode QS with its typical pattern of fast high frequencies and slower low frequencies (Moreau et al., 2020), a behavior that is further illustrated by the corresponding wavelet-decomposition spectrogram in Figure 8b.

https://doi.org/10.5194/egusphere-2026-2106
Preprint. Discussion started: 4 June 2026

Figure 9a shows three component geophone records of the first hammer shot at shot point 10 of the center line (Fig. A2). Using data from various azimuths the records exhibit the three predominant wave types in floating ice layers, and the arrivals can be analyzed at least up to 1 km distance. The first arrival is the undispersive quasi-symmetric QS_0 mode on the radial component that is followed by the horizontally polarized shear-mode SH_0 on the transverse component. The third arrival is the strongly dispersive quasi-Scholte mode QS on the vertical component. From these moveout patterns we estimate the velocity of the non-dispersive QS_0 and SH_0 modes as 3009 ± 60 m s^{-1} and 1638 ± 20 m s^{-1}, respectively, assuming 0.01 s pick accuracy (Table 3).

For natural icequake events the signal can be less strong. In the example in Figure 9b lower amplitudes result in a correspondingly lower signal-to-noise ratio, and the QS mode is not excited at all. Continuous geophone seismograms (Fig. 9c) indicate stronger seismic activity during the first half of the deployment until around 21 February 2025. The associated spectrogram indicate propagating energy in a broad frequency range between 0.4 and 1,000 Hz (Fig. 10a). These periods of high seismic activity last for several hours, and correlate with episodes of significant air temperature cooling events on 13, 16, 19, and 20 February 2025 (Fig. 10a). Figure 10b quantifies the frequency dependent correlation of high seismic energy with low temperatures. After 21 February 2025 the seismic activity is much lower. In the spectrograms we can discern daily variations of seismic activity, the more active periods are observed during day times. This suggests that the seismic activity of the lake ice layer is governed by the mechanical response to ambient air temperature variations.

At frequencies below 0.2 Hz the broadband data activity pattern differs compared to the higher frequencies (Fig. 10c). The pattern in the $0.03-0.2$ Hz range shows elevated amplitudes that last from several hours to several days. These episodes correlate with faster wind speeds (Figs. 10c, 2c) and wind gust speeds (Figs. 10c, A1a). The frequency dependent strength of the relationship is quantified in Figure 10c which shows correlation coefficients up to 0.8 between wind gust speed and seismic activity of the hourly sampled data.

The collective seismic response of the lake ice layer is summarized in example probabilistic power spectral density (PPSD) plots in Figure 11 for geophone data (top row) and broadband data (bottom row). Comparing the color-coded amplitudes of the spectrograms (Fig. 10a, c) to the PPSD amplitudes shows that energy above -100 dB at frequencies higher than 0.2 Hz is related to the active periods in the first half of the deployment. Energy at lower frequencies is associated to hydro-elastic propagation excited by local wind forcing (Valero Cano et al., 2026), and possibly microseisms.

3.2.3 Circular arrays beamforming

After these single sensor data examples we analyze the velocity and azimuth of seismic waves in the $1-3$ Hz frequency range using cross-correlation beamforming (Ruigrok et al., 2017) that we apply to one-hour vertical-component waveforms recorded by the three circular arrays. On average, seismic wave velocities range between 20 and 100 m s^{-1} associated with the obtained 10–50 s km^{-1} slowness (Fig. 12, Table 3). This is significantly slower compared to the QS_0 and SH_0 mode velocities estimated from the hammer shot moveout. However, these values are consistent with the velocity of quasi-Scholte waves (QS; Stein et al., 1998), suggesting that QS waves dominate vertical-component ice motions in the $1-3$ Hz frequency band. Our manual inspection indicates that, for the most part, the hourly average incidence direction differs for the three arrays, i.e., sources

https://doi.org/10.5194/egusphere-2026-2106
Preprint. Discussion started: 4 June 2026

Mode	Velocity (m s^{-1})	Frequency (Hz)	Data type
QS_0	3009±60	>5	radial component hammer shot data
SH_0	1638±20	>5	transversal component hammer shot data
QS_0	3380±140	2–24	RR ambient noise correlations
SH_0	1824±80	2–24	TT ambient noise correlations
QS	20–100	1–3	ZZ ambient noise correlation beamforming

Table 3. Seismic wave speed estimates of different modes obtained from different data types and with different methods. The QS_0 mode wave speed obtained from ZZ ambient noise correlations is 2850 ± 50 m s^{-1}.

vary on spatial scales that tend to be shorter compared to the inter-array distance. However, the arrays intermittently record energy that arrives from a consistent azimuth. Figure 12 shows beamforming results that indicate a coherent source region in the N225°E direction. This coincides with the major ice fracture or rift zone. The temporal variability of the associated wave field coherency suggests that circular beamforming data can be used to resolve the response pattern of this feature to environmental drivers. More generally, beamforming helps to investigate the distribution of ambient noise sources in the Lake Pääjärvi environment.

3.2.4 Ambient seismic noise correlations

We expect that the spatial variation of elastic ice properties can be imaged using ambient field correlation tomography, similar to crustal scale passive surface wave imaging. Here we explore the data quality of the ambient ice vibration correlations and estimate average wave propagation speeds and elastic moduli. We use 21 days of continuous waveforms recorded by the monotile geophone array to compute radial-radial (RR), transverse-transverse (TT), and vertical-vertical (ZZ) ambient noise correlations. We organize waveforms in daily segments, remove their mean, the linear trend, and the instrument response, and downsample to 100 Hz. We divide waveforms into half-hour segments and apply spectral whitening (Bensen et al., 2007) in the $1-30$ Hz frequency band. Following waveform rotation, we compute the daily RR, TT, and ZZ noise correlations between all station pairs, normalize them by their maximum value, and then linearly stack all noise correlations for the same station pair and component.

Figure 13 shows the RR, TT, and ZZ noise correlations filtered in two frequency bands. The gathers are constructed from all 21 945 station pairs. Correlations are stacked using a 50 m bin width. The RR and TT data (Fig. 13a, b, d, e) resolve system-scale propagation of high-SNR non-dispersive seismic arrivals on both correlation branches at all frequencies with average velocities of 3380 m s^{-1} and 1824 m s^{-1}, respectively (Table 3). The same values are obtained from the corresponding frequency-wavenumber (FK) spectra. Considering that quasi-symmetric QS_n waves dominate radial ice motions and horizontally-polarized shear waves SH_n govern transverse ice motions (Moreau et al., 2020), we infer that RR noise correlations exhibit QS_n propagation and TT noise correlations SH_n propagation. Here we observe the fundamental mode of these waves because the product of their frequency and ice thickness remains below 50 Hz·m (Moreau et al., 2020). In contrast, the ZZ correlations (Fig. 13c, f) show a distinct frequency dependence of the overall lower spatial coherence of the reconstructed

https://doi.org/10.5194/egusphere-2026-2106
Preprint. Discussion started: 4 June 2026

propagation. These moveout patterns and the corresponding FK spectra show, however, that the mode is not dispersive. The estimated speed of this low-SNR arrival is 2850 m s^{-1}. We interpret this to be motion associated with the longitudinally polarized QS_0 mode that also produces a small vertical displacement. We attribute the difference in wave speed estimates of this mode obtained from the RR and ZZ data to the different signal strengths. The energy partitioning across the two components is compatible with observed QS_0 icequake motion discussed below (Section 3.3).

The ZZ correlation gathers contain further a ∼330 m s^{-1} fast coherent acoustic signal that couples to the installed geophones and that can be observed at the kilometer scale. Acoustic energy can at least partially be attributed to the frequent operation of snowmobiles and all terrain vehicles on the lake ice for the deployment and station maintenance or recreational activities. Correlation gathers obtained with data from the three circular beamforming arrays and the 100 m long line array show the consistent reconstruction of the slow, dispersive QS mode discussed in Section 3.2.3, that we do not, however, reconstruct on the large lake array. This highlights the need for multiscale observations to resolve the rich elastic wavefield in seasonal floating lake ice.

The Poisson's ratio ν and Young's modulus E of a uniform, isotropic ice plate floating on a finite water column are (Stein et al., 1998)

$$\nu = 1 - 2\left(\frac{c_{\mathrm{SH}_0}}{c_{\mathrm{QS}_0}}\right)^2, \tag{1}$$

and

$$E = \rho\left(c_{\mathrm{QS}_0}\right)^2\left(1-\nu^2\right), \tag{2}$$

where c_{SH_0} is the velocity of SH_0 waves, c_{QS_0} is the velocity of QS_0 waves, and ρ is the ice density. Using an average $c_{\mathrm{SH}_0} = 1850$ m s^{-1} and $c_{\mathrm{QS}_0} = 3400$ m s^{-1} inferred from our noise correlations, and $\rho = 910$ kg m^{-3} (Moreau et al., 2020), we obtain $\nu = 0.42$ and $E = 8.59$ GPa. These values are near the upper limit of typical observations (Hunkins, 1960; Moreau et al., 2020), suggesting that the Lake Pääjärvi ice is comparatively stiff, which is compatible with the visual assessment and the interaction with the ice during the deployment.

3.2.5 DAS data and observations

We examine the power spectral density (PSD) of the DAS channels to assess the data quality and the frequency content of the recorded signals. The PSD derived from 24 hours of data recorded on 15 February 2025 (Fig. A3) exhibits discontinuities along the cable that coincide with the two bending points. For example, the contrasts marked by the red lines correspond to the coiled ends of the cable, and the contrast marked by the left black line corresponds to the first cable corner. The spectral power at 40−60 m along the cable is notably high below 0.1 Hz, likely because this cable segment lies on the lake shore and has poor coupling. The most energetic frequency bands are 0.1−1 Hz and 10−100 Hz. Examination of PSDs from other days show considerable spectral power variations in these two bands that are related to icequakes and other transient signals.

Our manual inspection of DAS waveforms in these two frequency bands yields hundreds of icequake detections with durations ranging from a few milliseconds to several seconds. Figure 14 shows an icequake record from 21:42 UTC on 19 February

https://doi.org/10.5194/egusphere-2026-2106
Preprint. Discussion started: 4 June 2026

2025. At frequencies below 10 Hz (Fig. 14a), dispersive QS waves with an apparent velocity between 10 and 50 m s^{-1} are observed at all DAS channels. QS propagation is not excited at frequencies above 10 Hz where the pattern is dominated by QS_0 and SH_0 modes with apparent velocities of 3400 and 1850 m s^{-1}, respectively (Fig. 14b). In both panels, the first seismic arrival appears at 615 m along the cable, which suggests the icequake is located in the vicinity of the N45°E trending second DAS cable segment, which can potentially be associated with field observations of a persistent long crack in this area. The frequency-wavenumber (FK) transforms (Fig. 14c, d) further illustrate that QS waves are dispersive while QS_0 and SH_0 waves are not. QS_0 waves are recorded along the entire cable, while SH_0 waves are absent in the second cable segment between 436 and 736 m. Because DAS systems are insensitive to motion orthogonal to the cable orientation, this suggests that SH_0 waves propagate predominantly perpendicular to the second cable segment.

We analyze the correspondence between the DAS strain-rate records and strain-rates derived from particle velocity measured by the 100 m long 26 geophone line array that we deployed along the cable. For this, we convert particle velocity to strain-rate using (Wang et al., 2018)

$$\dot{\epsilon}(x) = \frac{1}{L}\left[\dot{u}\left(x+\frac{L}{2}\right) - \dot{u}\left(x-\frac{L}{2}\right)\right]. \tag{3}$$

Equation 3 states that the strain-rate $\dot{\epsilon}$ at position x, averaged over the gauge length L, equals the difference of particle velocity $\dot{u}$ recorded at the gauge ends divided by L. Figure 14e compares a DAS strain-rate waveform recorded at 153.6 m to a strain-rate waveform derived from the two geophones that are closest to the corresponding DAS gauge ends. Although the signals represent strain-rate averaged over different spatial segments—the DAS gauge length is 9.6 m and the distance between the two used geophones is 8 m—, they show a consistent QS arrival. The colocated data have been used to correct the DAS system time stamping, and it can be further applied to calibrate DAS strain rate amplitude measurements and spatial gradient estimates from geophone data.

3.3 Acoustic wave field features

Strong acoustic icequake signals with 20 dB and more power above the background level were primarily observed during night times in the periods from 18 to 21 February 2025 and from 2 to 4 March 2025. Other periods were dominated by wind and other environmental noise. The one second long records of a representative icequake signal shown in Figure 15 illustrate the seismo-acoustic coupling. We estimate a backazimuth of 104° by rotating the horizontal geophone components to maximize the amplitudes of the QS_0 and SH_0 arrivals on the respective components. The vertical component seismic data (Fig. 15b) show the small-amplitude impulsive QS_0 arrival at 0.192 s that is followed by the dispersive QS mode with energy in the 20−500 Hz range starting at 0.24 s. The peak amplitude on the radial component (Fig. 15c) is now associated with the impulsive QS_0 arrival, and at 0.215 s the SH_0 mode dominates the transversal component (Fig. 15d).

The associated broadband acoustic signal (Fig. 15a) was recorded 15 m away from the line array geophone location. The acoustic signal corresponds to the geophone displacement record for frequencies for which the phase velocity in ice c_{ice} is larger than c_{air}, and shows the same dispersion in that high-frequency range. The dispersive acoustic signal transitions into a monochromatic wave train with a coincidence frequency $f_c \approx 120$ Hz. At f_c the two phase velocities match and the corre-

https://doi.org/10.5194/egusphere-2026-2106
Preprint. Discussion started: 4 June 2026

sponding equal wave lengths in ice and air lead to a resonance-like phenomenon and an efficient coupling of air waves that propagate with the speed of sound (Press et al., 1950; Schmelzbach et al., 2025). The monochromatic wave train ends at the arrival time of the direct air wave that propagates from the source to the microphone. We attribute the poorly expressed air wave arrival in our records compared to observations by Romeyn et al. (2021) and Schmelzbach et al. (2025) to higher environmental noise.

The duration δt_{ACW} of this monochromatic signal is proportional to the source-receiver distance (Schmelzbach et al., 2025). With a δt_{ACW} length of 0.165 s and an approximated group velocity $U_c^{QS} \approx 2\,c_{\mathrm{air}}$ (Press et al., 1950) of 600 m s^{-1} the source-receiver distance can be estimated to 99 m. Alternatively, we can use the standard S minus P travel time approach to constrain this distance. We can estimate the corresponding SH_0 minus QS_0 differential time from the observations of the QS_0 and SH_0 arrivals (Fig. 15c, d) and use the associated velocity measurements from Table 3. The values obtained from hammer shot data and noise correlation moveouts yield 83 m and 93 m, respectively, which agrees well with the δt_{ACW}-based estimate, in particular if we consider the 15 m distance between geophone and microphone.

The coincidence frequency is primarily controlled by the ice thickness h, the air temperature, and the elastic properties and density of water, ice, and air. Using Equation 15 in Romeyn et al. (2021) in a grid search and considering parameter values that are representative for the ambient conditions at Lake Pääjärvi, a frequency of $\sim$120 Hz corresponds to an ice thickness of 26 to 28 cm on 19 February 2025, which is again consistent with the in-situ measurements (Fig. 7). This consistency supports the deployment of acoustic sensors along the shore for passive estimates of average ice properties.

3.4 Ground Penetrating Radar sounding

Application of standard GPR travel time data processing yields the segmented reflection profile shown in Figure 5. The first D indicated arrival is the direct wave that propagates horizontally in the air between the source and receiver units of the GPR antenna. During the survey the ice was coated with a patchy snow cover not thicker than 2 cm that did not form a coherent snow-ice interface. The main arrival is the large amplitude reflection R at the ice-water interface at the base of the ice layer. After the R arrival, the reflection profile exhibits a ringing pattern likely associated with reflection multiples (Miners et al., 2002) within the ice layer. The average two-way zero-offset travel time τ is approximately 2.4 ns. With an average ice thickness of 22 cm, the electromagnetic (EM) wave velocity v is 0.18 m ns^{-1}. This is slightly higher than the 0.167 m ns^{-1} estimated for solid ice (Liu et al., 2014). Our larger velocities are compatible with properties of a softer ice layer containing entrapped air, as observed in the core samples (Section 3.6), which can increase the bulk EM wave propagation velocity. The generalized depth equation of the GPR is $h = c\tau/2/\sqrt{\varepsilon_r}$, where $c = 0.3$ m ns^{-1} is the velocity of the electromagnetic wave in vacuum (Liu et al., 2014). Together with the obtained estimates for v the dielectric constant is $\varepsilon_r \approx 2.68$, and this relatively low value has been associated with compact snow (Liu et al., 2014). This is consistent with our other observations of the lake ice characteristics that differ from sea ice.

We can resolve a decrease in the R reflection travel time from the first to the second segment, which coincides with the thinning of the ice illustrated in Figures 5 and 7a. The profile also resolves an increase in the travel time in the north-east bay which is compatible with the 30 cm thickness estimate at the time of the acquisition. The three central segments exhibit

https://doi.org/10.5194/egusphere-2026-2106
Preprint. Discussion started: 4 June 2026

stronger travel time fluctuations along the profile compared to the western and eastern segments. Such fluctuations are typically related to the ice thickness and the roughness of the ice-water interface (Liu et al., 2014), but the τ dependence on the dielectric constant implies that spatial heterogeneity in the ice properties affecting ε_r can also govern the observed travel time patterns. It seems plausible to use high-resolution seismic observations of h along a GPR profile in combination with ε_r dependent amplitude reflection coefficients to constrain ε_r as an indicator of the ice composition.

3.5 Hydroacoustic sounding observations

An example echogram derived from data collected over several hours on 11 February 2025 is shown in Figure 6c. While the data were processed using our standard workflow for wideband split-beam echosounder analysis, the unconventional deployment geometry necessitated additional processing steps to enable robust target tracking. Specifically, two transducers were operated sequentially and oriented at an angle of 45° relative to the vertical axis (Fig. 6a,b), producing a non-standard sampling geometry that complicates conventional single-beam target identification. The elongated streaks observed in the echogram likely indicate moving acoustic targets, primarily fish and potentially also rising gas bubbles. Discriminating between these target classes, however, requires further analysis. In particular, resolving the abundance and characteristics of bubble targets is essential for quantifying seafloor gas ebullition at the three sites (Fig. 6d).

3.6 Environmental Geochemistry analysis results

Figure 16a sketches the geochemical sampling strategy using the same symbols and colors as in panels (b) to (d) and in Figure 6d. We observed highest CH_4 concentrations around 10 to 1000 μmol L^{-1} in sediment porewater samples, with lower concentrations in water and ice samples, $\sim$0.01 to 0.1 μmol L^{-1} (Fig. 16c). However, all 161 measurements of dissolved CH_4 exceeded the calculated equilibrium value of 0.005 μmol L^{-1} at the time of sampling, indicating oversaturation and a potential flux of methane from the lake to the atmosphere. Concentrations of dissolved inorganic carbon DIC were similarly highest in the sediment porewaters, frequently in excess of 1000 μmol L^{-1}, and consistently 200$-$300 μmol L^{-1} in the water column (Fig. 16d). Gas volume in the ice was in the range 0$-$10% for all samples (Fig. 16b). A significant difference indicated by a Welch's t-statistic of 2.57 and $p = 0.013$ was observed between the upper 5 cm of the ice column (mean gas volume 2.99%) and the lower 5 cm (mean gas volume 1.43%).

4 Discussion

The diverse acquisition elements of our geophysical and geochemical experiments on 25 cm thick seasonal lake ice in southern Finland at $\sim$61°N include various seismic sensors deployed in different configurations, a fibre optic cable, a microphone, Ground Penetrating Radar (GPR), hydroacoustic sounding, manual ice thickness probing, environmental geochemistry sampling, and drone-assisted filming. Together, the different data types help establish reference observations for an effective resolution of evolving lake ice properties using seismic signals that can support lake system scale environmental monitoring.

https://doi.org/10.5194/egusphere-2026-2106
Preprint. Discussion started: 4 June 2026

The strongly dispersive QS mode and the weakly or non-dispersive QS_0 and HS_0 modes excited by hammer shots, icequakes, and environmental sources are observed to varying degree on the broadband sensors, geophones, the rotational seismic sensor, the fibre optic cable, and the microphone. The propagation speeds for the three modes inferred from beamforming and noise correlations range approximately between 20–100 m s^{-1}, 3000–3400 m s^{-1}, and 1650–1800 m s^{-1} (Table 3), respectively. We highlight the long range propagation of the longitudinally and transversely polarized QS_0 and HS_0 modes that support correlation based system-scale lake ice imaging. The dispersive QS mode leaks energy into the water column and is therefore reconstructed on shorter ranges. These differences imply the need of multi-scale sensing to resolve the full elastic wavefield in floating ice.

Array beamforming results obtained at three locations on the lake indicate spatio-temporally varying source regions of seismic energy. More detailed icequake excitation patterns to resolve evolving lake ice dynamics can be obtained by applying unsupervised detection and classification algorithms (Moreau et al., 2023) to the lake array geophone data. Many studies on icequake source mechanisms focus on events in or at the base of glaciers or ice sheets (Walter et al., 2010; Hudson et al., 2019, 2020; Chmiel et al., 2023; Umlauft et al., 2023). Data from the monotile lake array configuration is expected to improve our understanding of failure modes and the governing driving mechanisms in floating ice whose geometry differs from the thick sheets. The lake shore network collects observations to quantify the energy flux across the shore.

Our calibration of fibre optic cable signals with strain estimates along a geophone line array highlights the benefits of pooled sensor deployments, which can be important for icequake magnitude estimates (Moreau et al., 2023). This calibration principle can be applied to a comparison of array derived and direct rotational motion (Bernauer et al., 2021), which allows local estimates of wave propagation and ice properties. Our observations related to the resolution and sensitivity of the different colocated sensors, and the experience gained regarding experiment design and deployment logistics can inform the planning and execution of follow-up experiments on other lakes with similar characteristics.

In situ ice thickness measurements through auger holes yield values between 15 cm and 35 cm, with average values around 20 cm and 26 cm at the beginning and end of the seismic deployment in February and March 2025, respectively. These values and the spatial variations are compatible with the GPR reflection travel times and the GPR profile across the lake, and with the coincidence frequency-based seismo-acoustic thickness estimates. Moreover, the ice displayed a clear layered structure with basal horizons of harder primary and congelation ice overlain by softer superimposed ice as described by Leppäranta (2023). On average, the basal layers were in the order 25 cm thick and the superimposed layers 2–5 cm thick, although with significant spatial variability. Variable content of trapped gases between the two layers was evident from the estimation of density from the uppermost and lowermost 5 cm sections of the ice sheet. The lowermost 5 cm, extracted entirely from the basal ice, contains less trapped gas than the uppermost 5 cm (Fig. 16b), derived from a mixture of basal and superimposed ice. Variable thickness of the basal and superimposed layers throughout the lake may thus influence locally the physical properties of the ice.

On average, our initial estimates of the mean Poisson's ratio $\nu = 0.42$ and Young's modulus $E = 8.59$ GPa obtained from seismic noise correlations indicate high values compared to other cryo-environments (Hunkins, 1960; Moreau et al., 2020). Considering the high density contrast between methane gas (0.7 kg m^{-3}) and ice (900 kg m^{-3}), and that CH_4 gas bubbles are encapsulated during lake ice formation (Walter et al., 2006; Walter Anthony et al., 2010), wave propagation is expected to

https://doi.org/10.5194/egusphere-2026-2106
Preprint. Discussion started: 4 June 2026

be sensitive to CH_4 concentrations in ice. This suggests imaging of lateral variations of greenhouse gas concentrations from seismic data.

Emission of gas bubbles from sediments (ebullition) constitutes a substantial, albeit highly variable, fraction of the total aquatic CH_4 flux (Rosentreter et al., 2021). Ebullition may however exhibit significant spatial and temporal variability, not only between lakes but also within a single lake (Natchimuthu et al., 2016). Our geochemical analysis confirms an excess concentration of methane in the water column and ice samples of Lake Pääjärvi. However, concentrations in the ice samples in the order 0.01 to 0.1 μmol/L suggest that methane is only a minor constituent of the trapped gas in Pääjärvi lake ice. Rather, the higher concentrations of trapped gas in superimposed ice imply inclusion of air during secondary ice formation as a key determinant of ice density. Quantification of ebullition rates from sonar data is pending, but is expected to confirm low overall rates at the time of the experiment.

The intermittent, patchy (Fig. 4j), or absent snow cover during the approximately one month long field experiment offered many views of laterally variable ice properties across scales. This refers to bubbles from the millimeter to centimeter scale (Fig. 4i) which also exhibit various morphologies; crack patterns with crack lengths between millimeters and tens to hundreds of meters; and hundreds to thousands of irregularly shaped, opaque ice floes on the meter scale (Fig. 4h) that were frozen into a transparent black ice matrix that formed consistent macro-patterns on the kilometer scale. These patterns alternated with structurally more homogeneous sections, and the corresponding micro- and macro-properties combined, including possible effects of different gaseous phases, control the elastic wave propagation.

5 Conclusions

The notion that ice traps markers of environmental conditions that can be used to reconstruct past climate states underpins the analysis of ice cores collected in glaciers and ice sheets. Seasonal lake ice properties and responses differ in multiple ways from the thick glaciers, ice sheets, and also sea ice, but its evolving micro- and macroproperties similarly reflect the influence of the governing forces and environmental drivers. Our initial observations and results made on Lake Pääjärvi imply that icequake and ambient seismic wavefield tomography problems can be formulated to resolve ice thickness and elasticity parameters from elastic waves. This allows us to explore the resolution of spatially variable ice structure and composition using tomography. The obtained signals demonstrate the utility of active and passive seismic methods for studying aquatic systems at the system scale. The combined results from this and follow-up surveys, tomographic images, and ground truth observations are important for the integration and calibration of remote sensing and satellite observations (Engram et al., 2020; Boesch et al., 2021; Tsuruta et al., 2025; Kivimäki et al., 2025) for a more accurate and complete assessment of environmental processes.

Data availability. The dataset is available on https://doi.org/10.23729/fd-05823461-d7c4-3b8d-961a-9836b46e77ec (Strobel et al., 2026) after an embargo period that ends 1 May 2028.

https://doi.org/10.5194/egusphere-2026-2106
Preprint. Discussion started: 4 June 2026

Video supplement. The 15 minutes documentary is published on the University of Helsinki YouTube channel, https://youtu.be/KPWA8vkfZjc.

Author contributions. GH, TJ, JL, and CSt conceptualized the study and acquired funding. GH, JL, and FS administered the project. GH, TJ, LM, CSt, CSch, and YD developed the methodology. FS, RC, ASB, TV, MdL, TJ, YD, and EVC curated the data. Formal analysis was carried out by FS, EVC, TJ, MK, CSt, VDF, NR, RC, YD, and CSch. Field investigations were conducted by FS, GH, TJ, CSt, TO, JV, RC, MK, VDF, NR, YD, AR, ASB, LW, KA, VH, MAK, KK, EM, LN, EP, JT, and TV. Resources and instrumentation were provided by LW, CH, LM, OC, CSch, YD, TJ, CSt, and JL. Software development was performed by FS, LM, OC, EVC, AM, TV, and RC. Supervision was provided by GH, TJ, and CSt. Visualization was carried out by FS, EVC, YD, CSt, TJ, and MdL. FS, GH, CSt, TJ, AM, YD, CSch, EVC, and JL prepared the original manuscript draft. FS, GH, and TJ reviewed and edited the manuscript with input from all co-authors.

Competing interests. The contact author declares that no author has any competing interests.

Acknowledgements. The support staff of the University of Helsinki Lammi Biological Station is greatly acknowledged. We are grateful to the Foundation of the Heritage of All the Saints of Mount Athos for their logistical support. T. Luhta and P. Seipäjärvi participated in pilot deployments, and we thank S. Heinonen, K. Oinonen, J. Hällsten, T. Tiira, P. Uotila, and V. Naunin for their administrative, technical, and logistical support. We appreciate discussions with M. Isken about QGIS. This work was supported by the Research Council of Finland (Academy project DYNALake–dynamics of a frozen lake environment grant 362968, and Flagship of Advanced Mathematics for Sensing, Imaging, and Modelling grant 359182). We acknowledge the University of Helsinki IT4Science team for their support, and the computational and data storage resources of the Finnish Grid and Cloud Infrastructure (FGCI, urn:nbn:fi:research-infras-2016072533).

https://doi.org/10.5194/egusphere-2026-2106
Preprint. Discussion started: 4 June 2026

References

Arrigo, K. R., van Dijken, G., and Pabi, S.: Impact of a shrinking Arctic ice cover on marine primary production, Geophysical Research Letters, 35, https://doi.org/10.1029/2008GL035028, 2008.

Arst, H., Erm, A., Herlevi, A., Kutser, T., Leppäranta, M., Reinart, A., and Virta, J.: Optical properties of boreal lake waters in Finland and Estonia, Boreal Environment Research, 13, 133–158, 2008.

Arvola, L., Kankaala, P., Tulonen, T., and Ojala, A.: Effects of phosphorus and allochthonous humic matter enrichment on metabolic processes and community structure of plankton in a boreal lake (Lake Pääjärvi), Canadian Journal of Fisheries and Aquatic Sciences, 53, 1646–1662, https://doi.org/10.1139/f96-083, 1996.

Barry, R. G., Serreze, M. C., Maslanik, J. A., and Preller, R. H.: The Arctic Sea Ice-Climate System: Observations and modeling, Reviews of Geophysics, 31, 397–422, https://doi.org/10.1029/93RG01998, 1993.

Bensen, G. D., Ritzwoller, M. H., Barmin, M. P., Levshin, A. L., Lin, F., Moschetti, M. P., Shapiro, N. M., and Yang, Y.: Processing seismic ambient noise data to obtain reliable broad-band surface wave dispersion measurements, Geophysical Journal International, 169, 1239–1260, https://doi.org/10.1111/j.1365-246X.2007.03374.x, 2007.

Bernauer, F., Behnen, K., Wassermann, J., Egdorf, S., Igel, H., Donner, S., Stammler, K., Hoffmann, M., Edme, P., Sollberger, D., Schmelzbach, C., Robertsson, J., Paitz, P., Igel, J., Smolinski, K., Fichtner, A., Rossi, Y., Izgi, G., Vollmer, D., Eibl, E. P. S., Buske, S., Veress, C., Guattari, F., Laudat, T., Mattio, L., Sèbe, O., Olivier, S., Lallemand, C., Brunner, B., Kurzych, A. T., Dudek, M., Jaroszewicz, L. R., Kowalski, J. K., Bońkowski, P. A., Bobra, P., Zembaty, Z., Vackář, J., Málek, J., and Brokesova, J.: Rotation, Strain, and Translation Sensors Performance Tests with Active Seismic Sources, Sensors, 21, https://doi.org/10.3390/s21010264, 2021.

Beyreuther, M., Barsch, R., Krischer, L., Megies, T., Behr, Y., and Wassermann, J.: ObsPy: A Python Toolbox for Seismology, Seismological Research Letters, 81, 530–533, https://doi.org/10.1785/gssrl.81.3.530, 2010.

Boereboom, T., Depoorter, M., Coppens, S., and Tison, J.-L.: Gas properties of winter lake ice in Northern Sweden: implication for carbon gas release, Biogeosciences, 9, 827–838, https://doi.org/10.5194/bg-9-827-2012, 2012.

Boesch, H., Liu, Y., Tamminen, J., Yang, D., Palmer, P. I., Lindqvist, H., Cai, Z., Che, K., Di Noia, A., Feng, L., Hakkarainen, J., Ialongo, I., Kalaitzi, N., Karppinen, T., Kivi, R., Kivimäki, E., Parker, R. J., Preval, S., Wang, J., Webb, A. J., Yao, L., and Chen, H.: Monitoring Greenhouse Gases from Space, Remote Sensing, 13, https://doi.org/10.3390/rs13142700, 2021.

Brown, L. C. and Duguay, C. R.: The response and role of ice cover in lake-climate interactions, Progress in Physical Geography: Earth and Environment, 34, 671–704, https://doi.org/10.1177/0309133310375653, 2010.

Chmiel, M., Walter, F., Pralong, A., Preiswerk, L., Funk, M., Meier, L., and Brenguier, F.: Seismic Constraints on Damage Growth Within an Unstable Hanging Glacier, Geophysical Research Letters, 50, e2022GL102 007, https://doi.org/10.1029/2022GL102007, 2023.

Demer, D. A., Berger, L., Bernasconi, M., Bethke, E., Boswell, K., Chu, D., Domokos, R., Dunford, A., Fässler, S., Gauthier, S., Hufnagle, L. T., Jech, J. M., Bouffant, N., Lebourges-Dhaussy, A., Lurton, X., Macaulay, G. J., Perrot, Y., Ryan, T., Parker-Stetter, S., Stienessen, S., Weber, T., and Williamson, N.: Calibration of acoustic instruments, ICES Cooperative Research Reports (CRR), https://doi.org/10.17895/ices.pub.5494, 2015.

Engram, M., Walter Anthony, K. M., Sachs, T., Kohnert, K., Serafimovich, A., Grosse, G., and Meyer, F. J.: Remote sensing northern lake methane ebullition, Nature Climate Change, 10, 511–517, https://doi.org/10.1038/s41558-020-0762-8, 2020.

Finnish Environment Institute (SYKE): Lakes and rivers depth dataset (Järvien ja jokien syvyysaineisto), https://ckan.ymparisto.fi/dataset/jarvien-ja-jokien-syvyysaineisto, 2016.

https://doi.org/10.5194/egusphere-2026-2106
Preprint. Discussion started: 4 June 2026

Finnish Meteorological Institute: Meteorological observations, https://en.ilmatieteenlaitos.fi/download-observations, 2025.

Foote, K. G., Knudsen, H. P., Vestnes, G., MacLennan, D., and Simmonds, E.: Calibration of acoustic instruments for fish density estimation: a practical guide, ICES Cooperative Research Reports (CRR), https://doi.org/10.17895/ices.pub.8265, 1987.

Griffiths, K., Michelutti, N., Sugar, M., Douglas, M. S. V., and Smol, J. P.: Ice-cover is the principal driver of ecological change in High Arctic lakes and ponds, PLOS ONE, 12, 1–25, https://doi.org/10.1371/journal.pone.0172989, 2017.

Hakala, I., Huitu, E., Mäkelä, S., and Arvola, L.: Impacts of land-use on concentrations of nutrients in runoffs: Preliminary results in small catchment areas, Archiv für Hydrobiologie. Supplement Volumes, Monographic Studies, 13, 285–303, 2002.

Hillers, G., Koivisto, E., Haapanala, P., Kukkonen, I., Courbis, R., Ding, Y., Fordell, T., Heinonen, S., Junno, N., Juntunen, A. K., Komminaho, K., Kozlovskaya, E., Leveinen, J., Moisio, K., Näränen, J., Oksanen, T. J., Skyttä, P., Tanskanen, E., and Tiira, T.: FINNSIP - The mobile Finnish Seismic Instrument Pool, Seismica, 4, https://doi.org/10.26443/seismica.v4i1.1379, 2025.

Hudson, T. S., Smith, J., Brisbourne, A. M., and White, R. S.: Automated detection of basal icequakes and discrimination from surface crevassing, Annals of Glaciology, 60, 167–181, https://doi.org/10.1017/aog.2019.18, 2019.

Hudson, T. S., Brisbourne, A. M., Walter, F., Gräff, D., White, R. S., and Smith, A. M.: Icequake Source Mechanisms for Studying Glacial Sliding, Journal of Geophysical Research: Earth Surface, 125, e2020JF005 627, https://doi.org/10.1029/2020JF005627, 2020.

Hunkins, K.: Seismic studies of sea ice, Journal of Geophysical Research (1896-1977), 65, 3459–3472, https://doi.org/10.1029/JZ065i010p03459, 1960.

Igel, H., Cochard, A., Wassermann, J., Flaws, A., Schreiber, U., Velikoseltsev, A., and Pham Dinh, N.: Broad-band observations of earthquake-induced rotational ground motions, Geophysical Journal International, 168, 182–196, https://doi.org/10.1111/j.1365-246X.2006.03146.x, 2007.

Jilbert, T., Jokinen, S., Saarinen, T., Mattus-Kumpunen, U., Simojoki, A., Saarni, S., Salminen, S., Niemistö, J., and Horppila, J.: Impacts of a deep reactive layer on sedimentary phosphorus dynamics in a boreal lake recovering from eutrophication, Hydrobiologia, 847, 4401–4423, https://doi.org/10.1007/s10750-020-04289-9, 2020.

Kivimäki, E., Tenkanen, M., Aalto, T., Buchwitz, M., Luojus, K., Pulliainen, J., Rautiainen, K., Schneising, O., Sundström, A.-M., Tamminen, J., Tsuruta, A., and Lindqvist, H.: Environmental drivers constraining the seasonal variability in satellite-observed and modelled methane at northern high latitudes, Biogeosciences, 22, 5193–5230, https://doi.org/10.5194/bg-22-5193-2025, 2025.

Leppäranta, M.: Modelling the Formation and Decay of Lake Ice, in: The Impact of Climate Change on European Lakes, edited by George, G., pp. 63–83, Springer Netherlands, Dordrecht, ISBN 978-90-481-2945-4, https://doi.org/10.1007/978-90-481-2945-4_5, 2010.

Leppäranta, M.: Structure and Properties of Lake Ice, pp. 63–108, Springer International Publishing, Cham, ISBN 978-3-031-25605-9, https://doi.org/10.1007/978-3-031-25605-9_3, 2023.

Li, J., Roche, B., Bull, J. M., White, P. R., Leighton, T. G., Provenzano, G., Dewar, M., and Henstock, T. J.: Broadband Acoustic Inversion for Gas Flux Quantification—Application to a Methane Plume at Scanner Pockmark, Central North Sea, Journal of Geophysical Research: Oceans, 125, e2020JC016 360, https://doi.org/10.1029/2020JC016360, 2020.

Liu, H., Takahashi, K., and Sato, M.: Measurement of Dielectric Permittivity and Thickness of Snow and Ice on a Brackish Lagoon Using GPR, IEEE Journal of Selected Topics in Applied Earth Observations and Remote Sensing, 7, 820–827, https://doi.org/10.1109/JSTARS.2013.2266792, 2014.

Matsumoto, M., Yoshimura, M., Naoki, K., Cho, K., and Wakabayashi, H.: Ground penetrating radar data interpretation using electromagnetic field analysis for sea ice thickness measurement, The International Archives of the Photogrammetry, Remote Sensing and Spatial Information Sciences, XLII-3-W7, 47–50, https://doi.org/10.5194/isprs-archives-XLII-3-W7-47-2019, 2019.

https://doi.org/10.5194/egusphere-2026-2106
Preprint. Discussion started: 4 June 2026

Mellor, M.: Ship resistance in thick brash ice, Cold Regions Science and Technology, 3, 305–321, https://doi.org/10.1016/0165-232X(80)90037-3, 1980.

Meng, X., Zhu, Z., Liu, H., Lian, Y., Lu, H., Wang, Y., Shi, R., and Spencer, B. F.: A Drone-Borne GPR System for Lake and River Ice Thickness Monitoring, Water Resources Research, 61, e2025WR040 290, https://doi.org/10.1029/2025WR040290, 2025.

Michel, B. and Ramseier, R. O.: Classification of river and lake ice, Canadian Geotechnical Journal, 8, 36–45, https://doi.org/10.1139/t71-004, 1971.

Miners, W. D., Wolff, E. W., Moore, J. C., Jacobel, R., and Hempel, L.: Modeling the radio echo reflections inside the ice sheet at Summit, Greenland, Journal of Geophysical Research: Solid Earth, 107, EPM 6–1–EPM 6–11, https://doi.org/10.1029/2001JB000535, 2002.

Mordret, A. and Grushin, A. G.: Beating the aliasing limit with aperiodic monotile arrays, Physical Review Applied, 23, 034 021, https://doi.org/10.1103/PhysRevApplied.23.034021, 2025.

Moreau, L., Boué, P., Serripierri, A., Weiss, J., Hollis, D., Pondaven, I., Vial, B., Garambois, S., Larose, É., Helmstetter, A., Stehly, L., Hillers, G., and Gilbert, O.: Sea Ice Thickness and Elastic Properties From the Analysis of Multimodal Guided Wave Propagation Measured With a Passive Seismic Array, Journal of Geophysical Research: Oceans, 125, e2019JC015 709, https://doi.org/10.1029/2019JC015709, 2020.

Moreau, L., Seydoux, L., Weiss, J., and Campillo, M.: Analysis of microseismicity in sea ice with deep learning and Bayesian inference: application to high-resolution thickness monitoring, The Cryosphere, 17, 1327–1341, https://doi.org/10.5194/tc-17-1327-2023, 2023.

Natchimuthu, S., Sundgren, I., Gålfalk, M., Klemedtsson, L., Crill, P., Danielsson, Å., and Bastviken, D.: Spatio-temporal variability of lake CH4 fluxes and its influence on annual whole lake emission estimates, Limnology and Oceanography, 61, S13–S26, https://doi.org/10.1002/lno.10222, 2016.

Palosuo, E.: Frozen Slush on Lake Ice, Geophysica, 9, 1965.

Perovich, D. K. and Polashenski, C.: Albedo evolution of seasonal Arctic sea ice, Geophysical Research Letters, 39, https://doi.org/10.1029/2012GL051432, 2012.

Press, F., Ewing, M., Crary, A. P., Katz, S., and Oliver, J.: Air-coupled flextural waves in floating ice, Geophysical research papers, 6, 1950.

QGIS Development Team: QGIS Geographic Information System, Open Source Geospatial Foundation, http://qgis.org, 2009.

Rissanen, A. J., Jilbert, T., Simojoki, A., Mangayil, R., Aalto, S. L., Khanongnuch, R., Peura, S., and Jäntti, H.: Organic matter lability modifies the vertical structure of methane-related microbial communities in lake sediments, Microbiology Spectrum, 11, e01 955–23, https://doi.org/10.1128/spectrum.01955-23, 2023.

Romeyn, R. and Hanssen, A.: Microphone recording of flexural waves for estimation of lake ice thickness, Cold Regions Science and Technology, 211, 103 875, https://doi.org/10.1016/j.coldregions.2023.103875, 2023.

Romeyn, R., Hanssen, A., Ruud, B. O., and Johansen, T. A.: Sea ice thickness from air-coupled flexural waves, The Cryosphere, 15, 2939–2955, https://doi.org/10.5194/tc-15-2939-2021, 2021.

Rosentreter, J. A., Borges, A. V., Deemer, B. R., Holgerson, M. A., Liu, S., Song, C., Melack, J., Raymond, P. A., Duarte, C. M., Allen, G. H., Olefeldt, D., Poulter, B., Battin, T. I., and Eyre, B. D.: Half of global methane emissions come from highly variable aquatic ecosystem sources, Nature Geoscience, 14, 225–230, https://doi.org/10.1038/s41561-021-00715-2, 2021.

Rossi, Y., Bernauer, F., Lin, C.-J., Guattari, F., and Pinot, B.: Quantifying Rotation-Induced Errors in Near-Field Seismic Recordings: Assessing Impact on Rotation and Acceleration Measurements, Seismica, 4, https://doi.org/10.26443/seismica.v4i1.1444, 2025.

Ruigrok, E., Gibbons, S., and Wapenaar, K.: Cross-correlation beamforming, Journal of Seismology, 21, 495–508, https://doi.org/10.1007/s10950-016-9612-6, 2017.

https://doi.org/10.5194/egusphere-2026-2106
Preprint. Discussion started: 4 June 2026

Ruuhijärvi, R.: A general description of the oligotrophic lake Pääjärvi, southern Finland, and the ecological studies on it, Annales Botanici Fennici, 11, 95–104, 1974.

Schmelzbach, C., May, D., Wetter, C., Stähler, S., and Clinton, J.: Monitoring lake ice with seismic and acoustic sensors, in: EGU General Assembly 2022, pp. EGU22–12 233, Vienna, Austria, https://doi.org/10.5194/egusphere-egu22-12233, 2022.

Schmelzbach, C., Wetter, C., and Stähler, S. C.: The Sound of Ice: Characterising Lake Ice using Seismo-Acoustic Observations, in: NSG 2025: 31st Meeting of Environmental and Engineering Geophysics, vol. 2025, pp. 1–5, European Association of Geoscientists & Engineers, https://doi.org/10.3997/2214-4609.202520265, 2025.

Schreiber, K. U., Hautmann, J. N., Velikoseltsev, A., Wassermann, J., Igel, H., Otero, J., Vernon, F., and Wells, J.-P. R.: Ring Laser Measurements of Ground Rotations for Seismology, Bulletin of the Seismological Society of America, 99, 1190–1198, https://doi.org/10.1785/0120080171, 2009.

Simola, H. and Uimonen-Simola, P.: Recent stratigraphy and accumulation of sediment in the deep, oligotrophic Lake Pääjärvi in South Finland, Hydrobiologia, 103, 287–293, https://doi.org/10.1007/BF00028468, 1983.

Singarayer, J. S., Bamber, J. L., and Valdes, P. J.: Twenty-First-Century Climate Impacts from a Declining Arctic Sea Ice Cover, Journal of Climate, 19, 1109 – 1125, https://doi.org/10.1175/JCLI3649.1, 2006.

Smith, D., Myers, J. S., Kaplan, C. S., and Goodman-Strauss, C.: An aperiodic monotile, Combinatorial Theory, 4, https://doi.org/10.5070/C64163843, 2024a.

Smith, D., Myers, J. S., Kaplan, C. S., and Goodman-Strauss, C.: A chiral aperiodic monotile, Combinatorial Theory, 4, https://doi.org/10.5070/C64264241, 2024b.

Stein, P. J., Euerle, S. E., and Parinella, J. C.: Inversion of pack ice elastic wave data to obtain ice physical properties, Journal of Geophysical Research: Oceans, 103, 21 783–21 793, https://doi.org/10.1029/98JC01269, 1998.

Stocker, B., Roth, R., Joos, F., et al.: Multiple greenhouse-gas feedbacks from the land biosphere under future climate change scenarios, Nature Climate Change, 3, 666–672, https://doi.org/10.1038/nclimate1864, 2013.

Strobel, F., Hillers, G., Jilbert, T., Loehr, J., Stranne, C., Oksanen, T., Vänskä, J., Courbis, R., Rintamäki, A., Sadeghi-Bagherabadi, A., Weißgräber, L., Ding, Y., de Langenhagen, M., Valero Cano, E., Atobra, K., Doñate Felip, V., Hopiavuori, V., Kankainen, M., Khodadadi, M. A., Kolehmainen, K., Makkonen, E., Nygrén, L., Purhonen, E., Rolleberg, N., Tuomiranta, J., Vuorinen, T., Mordret, A., Schmelzbach, C., Moreau, L., Coutant, O., and Hadziioannou, C.: The DYNALake project dataset, https://doi.org/10.23729/fd-05823461-d7c4-3b8d-961a-9836b46e77ec, Version 1.0, 2026.

Tsuruta, A., Kuze, A., Shiomi, K., Kataoka, F., Kikuchi, N., Aalto, T., Backman, L., Kivimäki, E., Tenkanen, M. K., McKain, K., García, O. E., Hase, F., Kivi, R., Morino, I., Ohyama, H., Pollard, D. F., Sha, M. K., Strong, K., Sussmann, R., Te, Y., Velazco, V. A., Vrekoussis, M., Warneke, T., Zhou, M., and Suto, H.: Global CH_4 fluxes derived from JAXA/GOSAT lower-tropospheric partial column data and the CarbonTracker Europe-CH_4 atmospheric inverse model, Atmospheric Chemistry and Physics, 25, 7829–7862, https://doi.org/10.5194/acp-25-7829-2025, 2025.

Umlauft, J., Johnson, C. W., Roux, P., Trugman, D. T., Lecointre, A., Walpersdorf, A., Nanni, U., Gimbert, F., Rouet-Leduc, B., Hulbert, C., Lüdtke, S., Marton, S., and Johnson, P. A.: Mapping Glacier Basal Sliding Applying Machine Learning, Journal of Geophysical Research: Earth Surface, 128, e2023JF007 280, https://doi.org/10.1029/2023JF007280, 2023.

Valero Cano, E., Moreau, L., Strobel, F., and Hillers, G.: Using flexural waves recorded by distributed acoustic sensing to infer the ice thickness and water depth of a frozen lake, in: EGU General Assembly 2026, pp. EGU26–16 347, Vienna, Austria, https://doi.org/10.5194/egusphere-egu26-16347, 2026.

https://doi.org/10.5194/egusphere-2026-2106
Preprint. Discussion started: 4 June 2026

Valpola, S. E. and Ojala, A. E.: Post-glacial sedimentation rate and patterns in six lakes of the Kokemäenjoki upper watercourse, Finland, Boreal environment research, 11, 195, https://doi.org/10.60910/tp1b-tyk7, 2006.

Vincent, W. F., Callaghan, T. V., Dahl-Jensen, D., Johansson, M., Kovacs, K. M., Michel, C., Prowse, T., Reist, J. D., and Sharp, M.: Ecological Implications of Changes in the Arctic Cryosphere, AMBIO, 40, 87–99, https://doi.org/10.1007/s13280-011-0218-5, 2011.

Walter, F., O'Neel, S., McNamara, D., Pfeffer, W. T., Bassis, J. N., and Fricker, H. A.: Iceberg calving during transition from grounded to floating ice: Columbia Glacier, Alaska, Geophysical Research Letters, 37, https://doi.org/10.1029/2010GL043201, 2010.

Walter, K. M., Zimov, S. A., Chanton, J. P., Verbyla, D., and Chapin, F. S.: Methane bubbling from Siberian thaw lakes as a positive feedback to climate warming, Nature, 443, 71–75, https://doi.org/10.1038/nature05040, 2006.

Walter Anthony, K. M., Vas, D. A., Brosius, L., Chapin III, F. S., Zimov, S. A., and Zhuang, Q.: Estimating methane emissions from northern lakes using ice-bubble surveys, Limnology and Oceanography: Methods, 8, 592–609, https://doi.org/10.4319/lom.2010.8.0592, 2010.

Wang, H. F., Zeng, X., Miller, D. E., Fratta, D., Feigl, K. L., Thurber, C. H., and Mellors, R. J.: Ground motion response to an ML 4.3 earthquake using co-located distributed acoustic sensing and seismometer arrays, Geophysical Journal International, 213, 2020–2036, https://doi.org/10.1093/gji/ggy102, 2018.

Weidner, E., Weber, T. C., Mayer, L., Jakobsson, M., Chernykh, D., and Semiletov, I.: A wideband acoustic method for direct assessment of bubble-mediated methane flux, Continental Shelf Research, 173, 104–115, https://doi.org/10.1016/j.csr.2018.12.005, 2019.

Weiss, R. F. and Price, B. A.: Nitrous oxide solubility in water and seawater, Marine Chemistry, 8, 347–359, https://doi.org/10.1016/0304-4203(80)90024-9, 1980.

Wetter, C., Schmelzbach, C., and Stähler, S. C.: Monitoring lake ice with acoustic sensors, in: EGU General Assembly 2023, pp. EGU23–10 127, Vienna, Austria, https://doi.org/10.5194/egusphere-egu23-10127, 2023.

Wiesenburg, D. A. and Guinasso, N. L. J.: Equilibrium solubilities of methane, carbon monoxide, and hydrogen in water and sea water, Journal of Chemical & Engineering Data, 24, 356–360, https://doi.org/10.1021/je60083a006, 1979.

Xing, J., Song, R., Zhen, S., and Jiang, X.: Construction of the Central Arctic Sea Ice Structure and Acoustic Velocity Model at the Short-Term Ice Station During N11 CHINARE, IEEE Transactions on Geoscience and Remote Sensing, 60, 1–7, https://doi.org/10.1109/TGRS.2021.3107363, 2022.

https://doi.org/10.5194/egusphere-2026-2106
Preprint. Discussion started: 4 June 2026

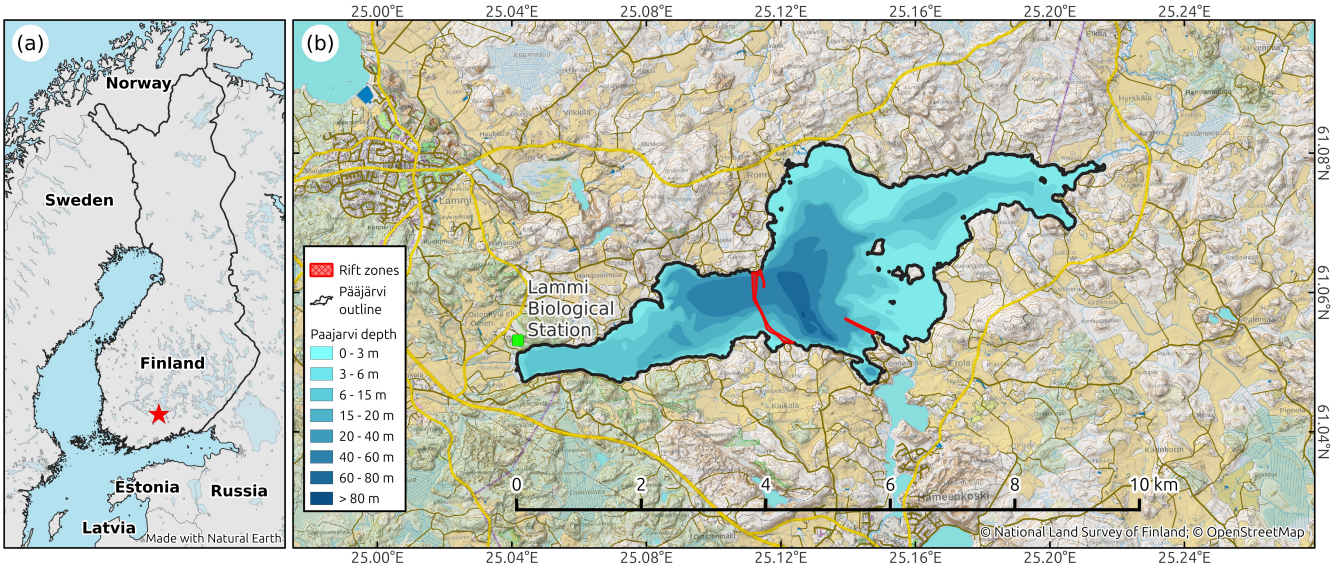

Figure 1. (a) The location of Lake Pääjärvi in southern Finland. (b) The environment of Lake Pääjärvi features elevations on the tens of meters scale. The town of Lammi is located in the upper left. Bathymetry data are from the Finnish Environment Institute (SYKE) (2016).

https://doi.org/10.5194/egusphere-2026-2106
Preprint. Discussion started: 4 June 2026

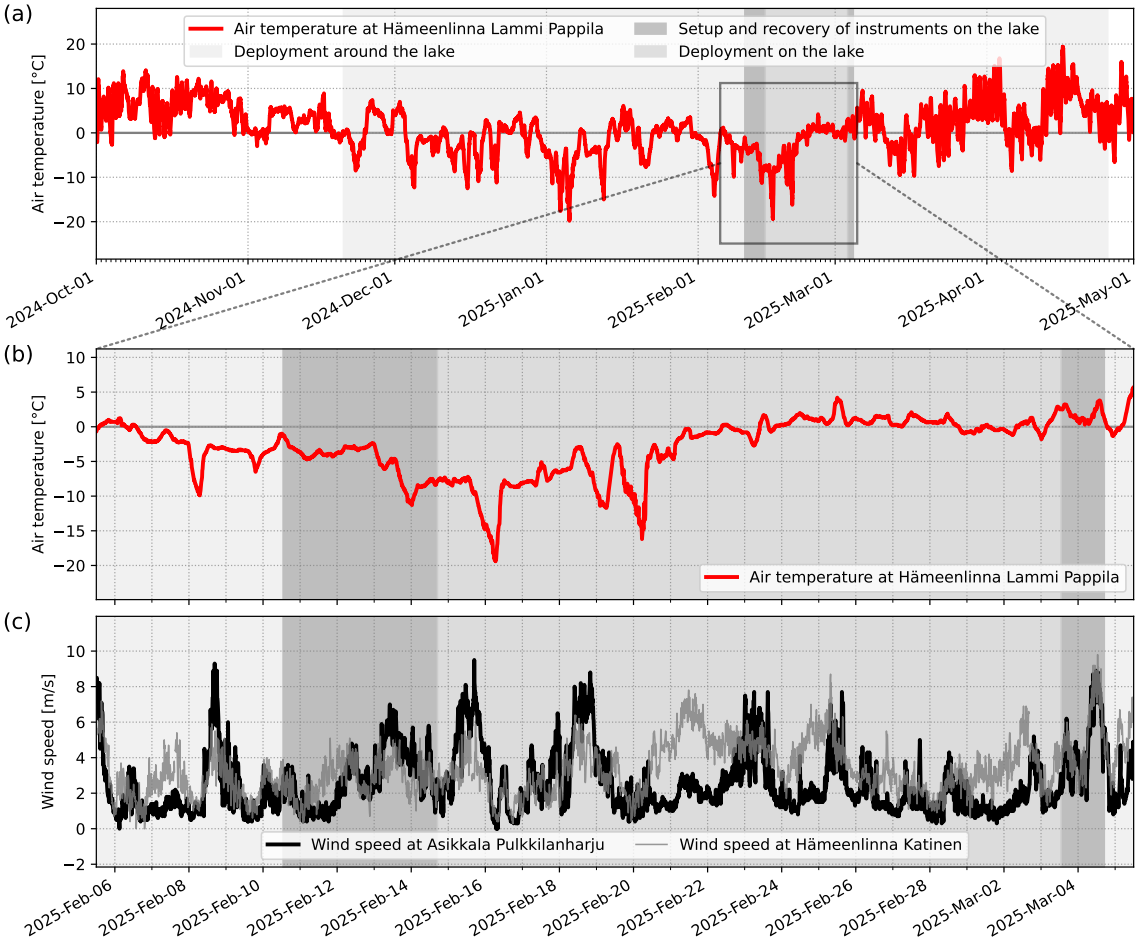

Figure 2. Most relevant meteorological data. (a) The air temperature is measured at Lammi Biological Station. Shades of gray indicate deployment phases. (b) Zoom-in on the temperature profile during the deployment on the lake. (c) The wind speed records obtained during the same time window are measured at stations Sikkala Pulkkilanharju and Hämeenlinna Katinen that are located about 30 km north-west and 35 km west of Lake Pääjärvi, respectively.

https://doi.org/10.5194/egusphere-2026-2106
Preprint. Discussion started: 4 June 2026

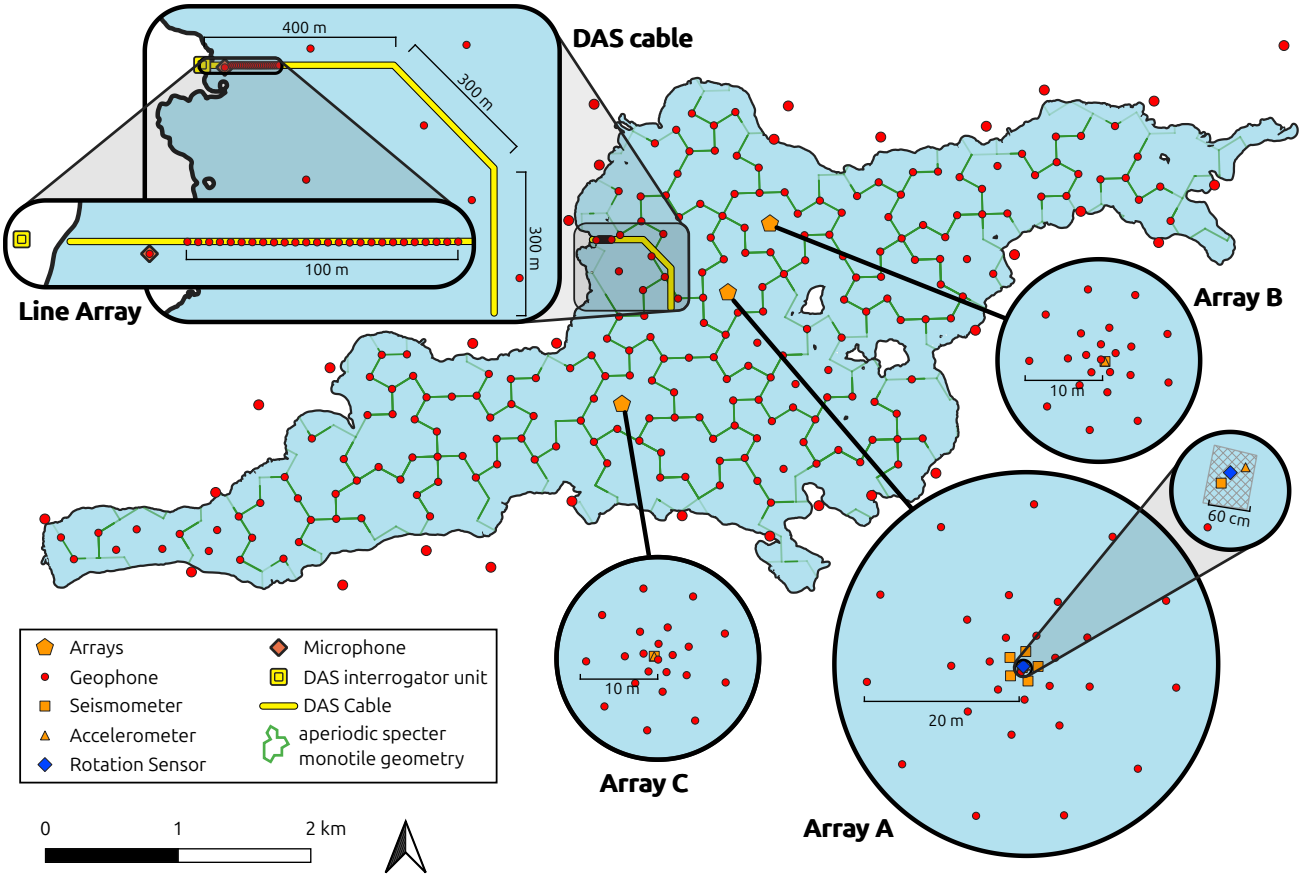

Figure 3. Overview of the seismic deployment elements including the lake shore network, the monotile lake ice array, the three circular arrays, and the line array along the fibre-optic cable of the Distributed Acoustic Sensing system.

https://doi.org/10.5194/egusphere-2026-2106
Preprint. Discussion started: 4 June 2026

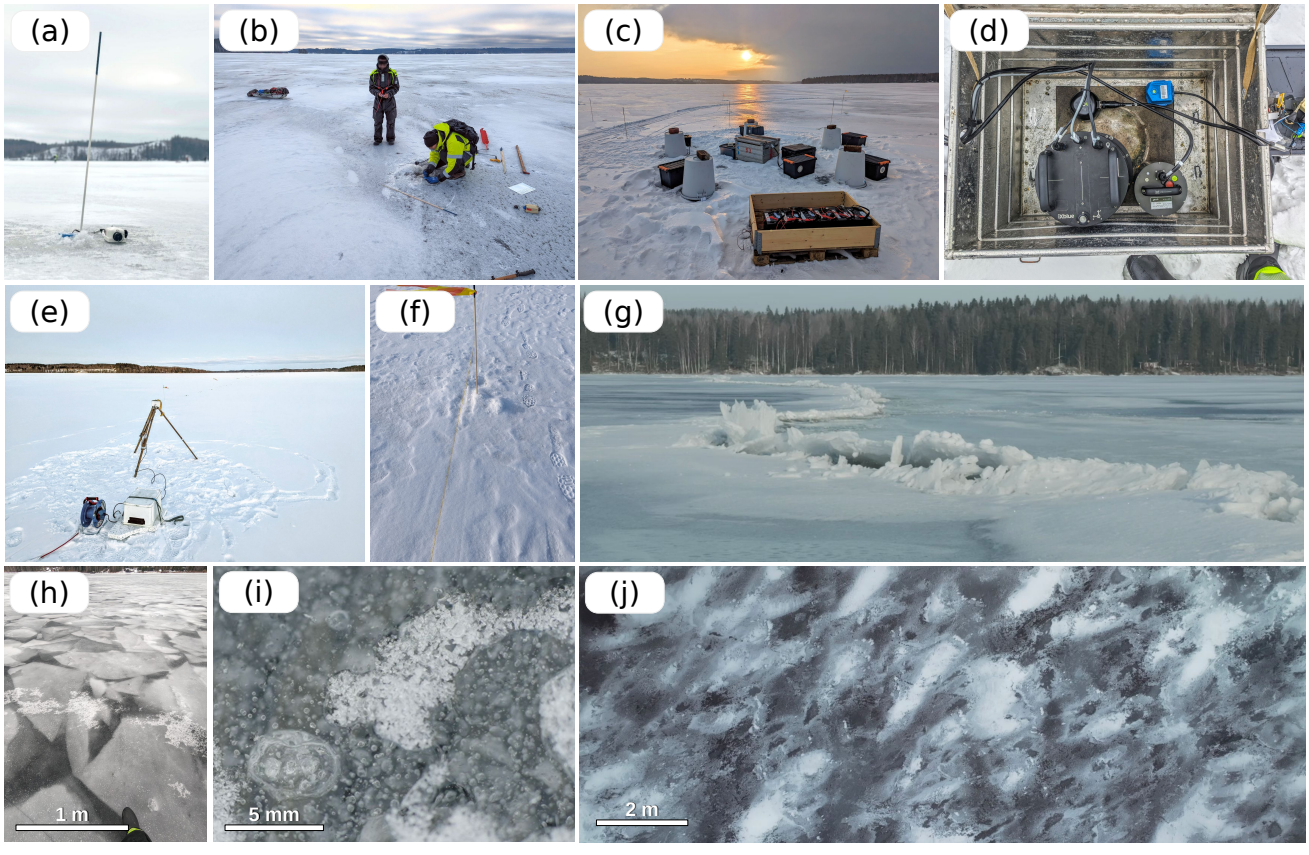

Figure 4. Impressions from the ice deployment. (a) An installed geophone (blue) with GSB data logger (white). (b) A geophone is installed on the ice. (c) The center of Array A with seismometers under the white buckets. Batteries and data loggers are stored in the black boxes. The six batteries on the pallet are powering the rotational seismometer in the aluminum box. (d) Inside the aluminum box are the rotational seismometer (lower left), a seismometer (lower right), an accelerometer (upper left), and a geophone (upper right). (e) The microphone array box is mounted on a tripod at 70 cm above the ground. The line array and marking sticks along the DAS cable are visible in the background. (f) The fibre optic cable lies on the snowy surface of the ice. (g) The rift zone (Fig. 1). The view is to the north. (h–j) Impressions of the spatially variable structure and composition of the ice at different scales.

https://doi.org/10.5194/egusphere-2026-2106
Preprint. Discussion started: 4 June 2026

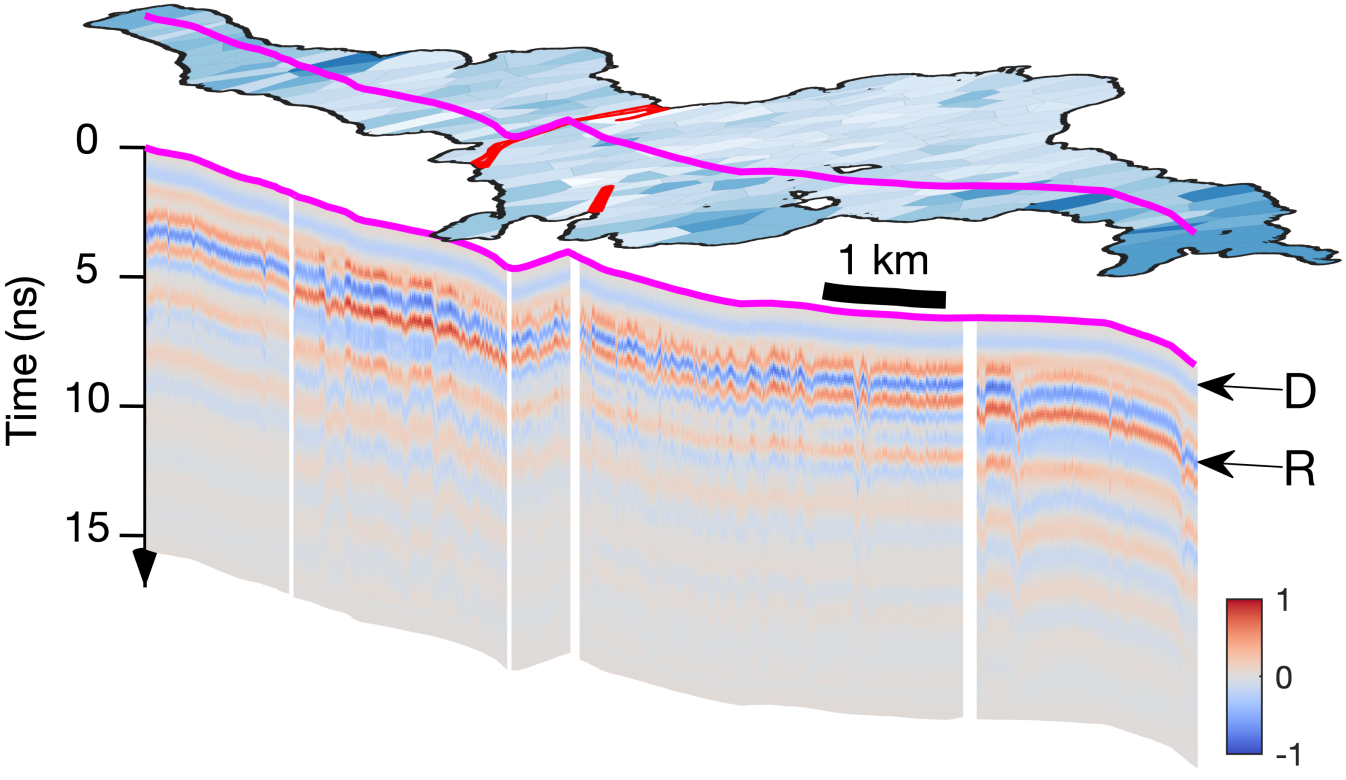

Figure 5. Ground Penetrating Radar (GPR) observations along the purple indicated profile across the lake. The blue colors on top reproduce the in-situ ice thickness measurements shown in Figure 7a, and the red areas mark the rift zones indicated in Figure 1b. The radargram of the GPR measurements is plotted along the transect. A direct wave (D) between the transmitter and the receiver antenna appears as a continuous horizon across all five segments. The ice-water interface reflection (R) indicates variations in ice thickness and properties.

https://doi.org/10.5194/egusphere-2026-2106
Preprint. Discussion started: 4 June 2026

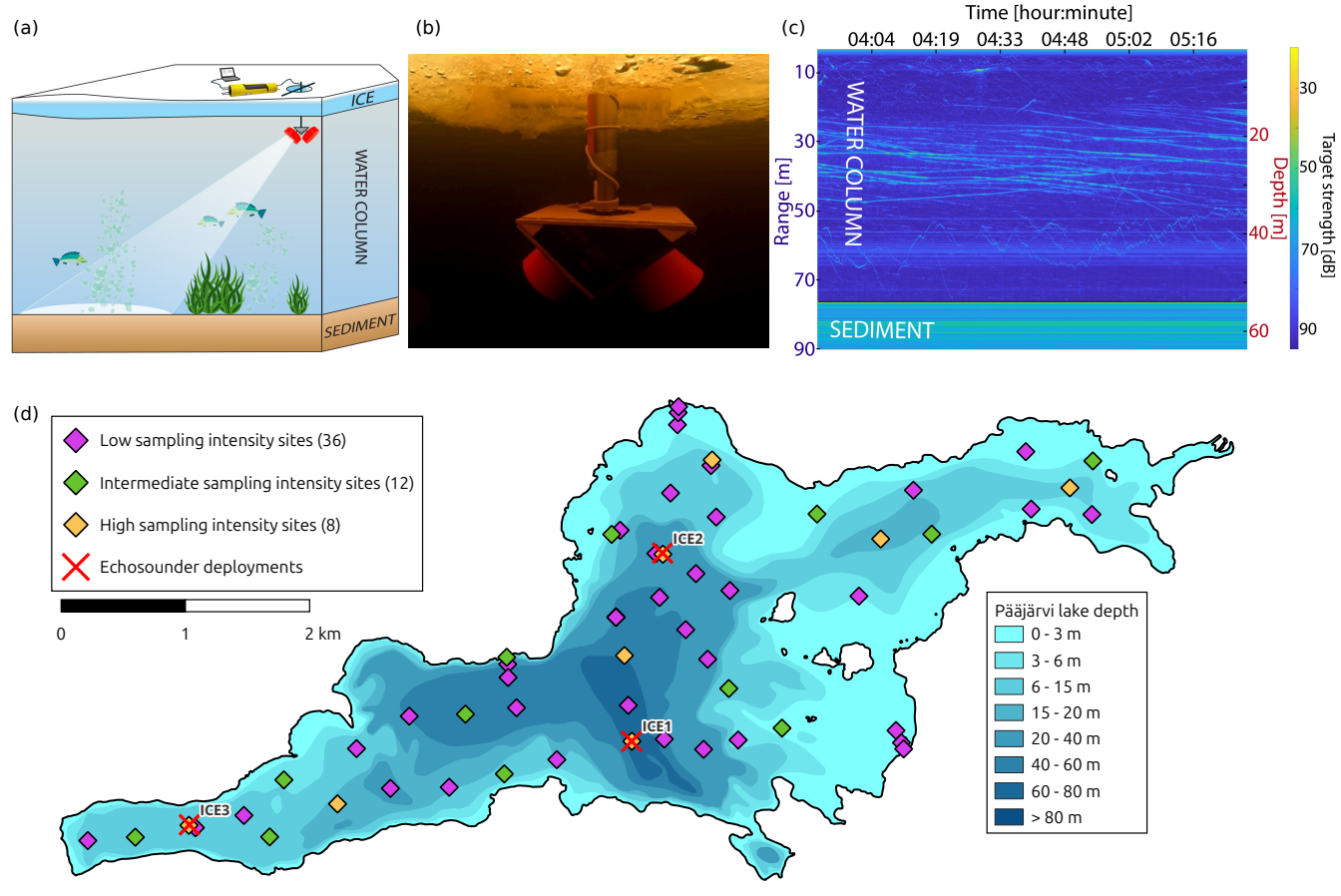

Figure 6. (a) The cartoon of the hydroacoustic sounding experiment refers to the sounding system, including a laptop, a 4G-modem, and the power supply on the ice, and to monitoring targets in the water column. (b) The two transducers of the echosounding system operate below the ice. (c) Reflection signals obtained with the echosounder. (d) Locations of the 56 geochemical sampling sites and the three echosounder deployments. At low sampling intensity sites (purple) only soft and hard ice layer thickness are measured. Intermediate sampling intensity sites (green) add measurements of CH_4 concentrations in ice. High sampling intensity sites (yellow) add again measurements of CH_4 concentrations in water and sediments, dissolved inorganic carbon in water and sediments, and temperature and dissolved oxygen in water.

https://doi.org/10.5194/egusphere-2026-2106
Preprint. Discussion started: 4 June 2026

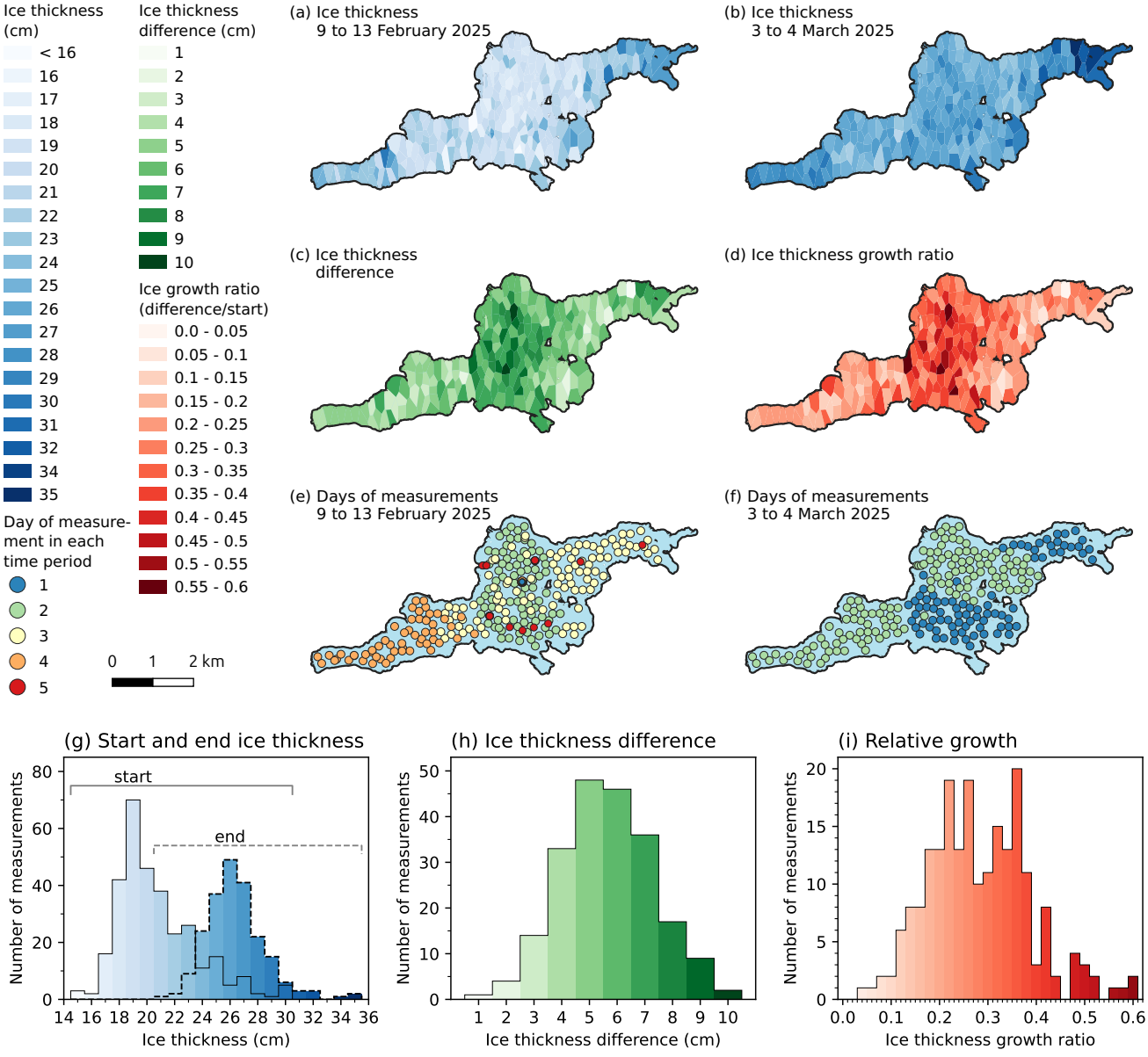

Figure 7. Ice thickness data. Ice thickness was measured during the (a) deployment and (b) during the retrieval of the instruments on the ice at every geophone location. We conducted the measurements within (e) a five day window and (f) a two day window respectively. Histograms of the (g) thickness measurements, (h) the thickness difference, and (i) the relative growth.

https://doi.org/10.5194/egusphere-2026-2106
Preprint. Discussion started: 4 June 2026

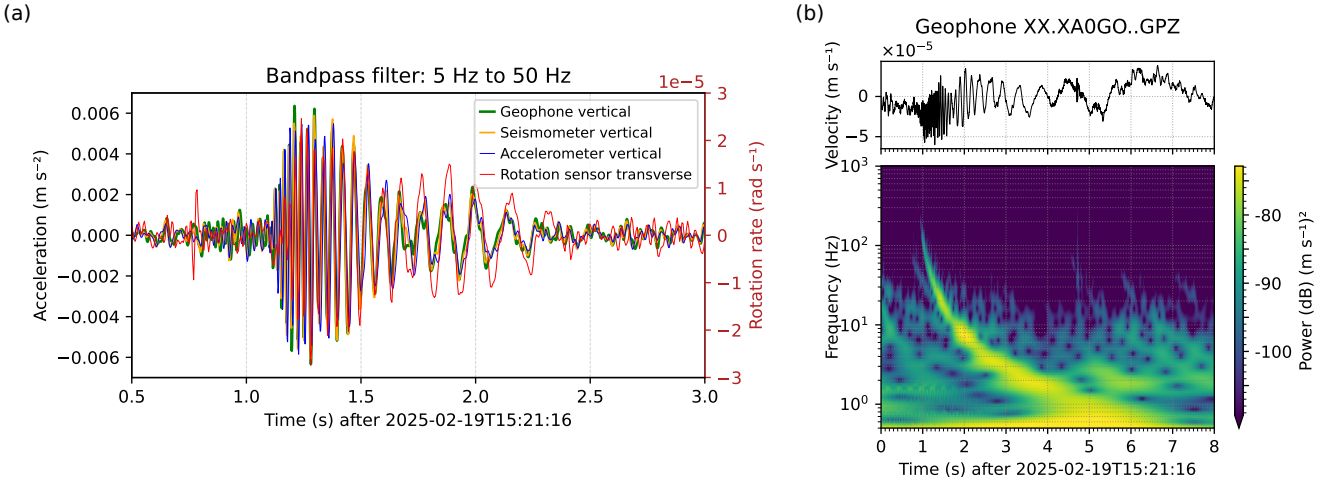

Figure 8. Bandpass filtered waveforms and a spectrogram of a hammer shot recorded with multiple instruments. The hammer shot was applied at location 10 in the center line in Figure A2. (a) Waveforms recorded with multiple co-located instruments at Array A (Fig. 3). The geophone (green) and seismometer (yellow) velocity records are differentiated in time to match the accelerometer (blue) data and to be in phase with the rotational (red) data. The waveforms are consistent and show the typical dispersive pattern of the QS mode. (b) The broadband record of the geophone and its wavelet spectrogram show the dispersive nature of the QS mode.

https://doi.org/10.5194/egusphere-2026-2106
Preprint. Discussion started: 4 June 2026

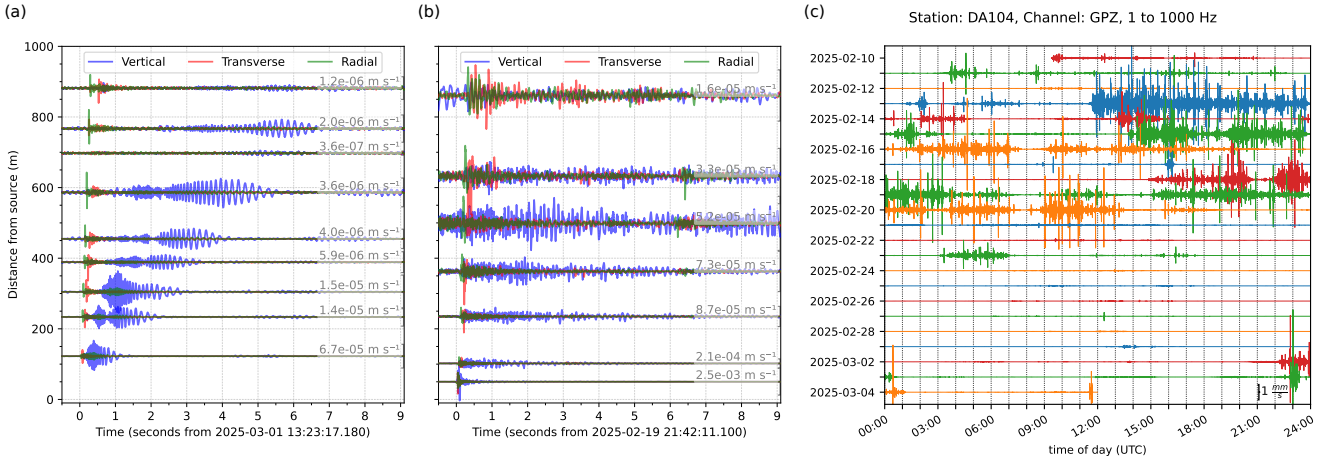

Figure 9. Seismic data examples. (a) Hammer shot signals from location 10 of the center line show the three QS_0 (green), SH_0 (red), and QS (blue) modes on different components. The station at ∼700 m shows a much smaller signal because the sensor is located behind an island. (b) Corresponding signals of an icequake. The amplitudes in panels (a) and (b) are scaled by the squared distance to the source for better visibility. (c) Vertical component record of the full 23-day dataset of station DA104 in the central part of the lake exhibit intermitted sequences of high seismic activity in the first half of the deployment, and a quiet period in the second half. We observe this pattern consistently at all on-ice stations across the whole lake.

https://doi.org/10.5194/egusphere-2026-2106
Preprint. Discussion started: 4 June 2026

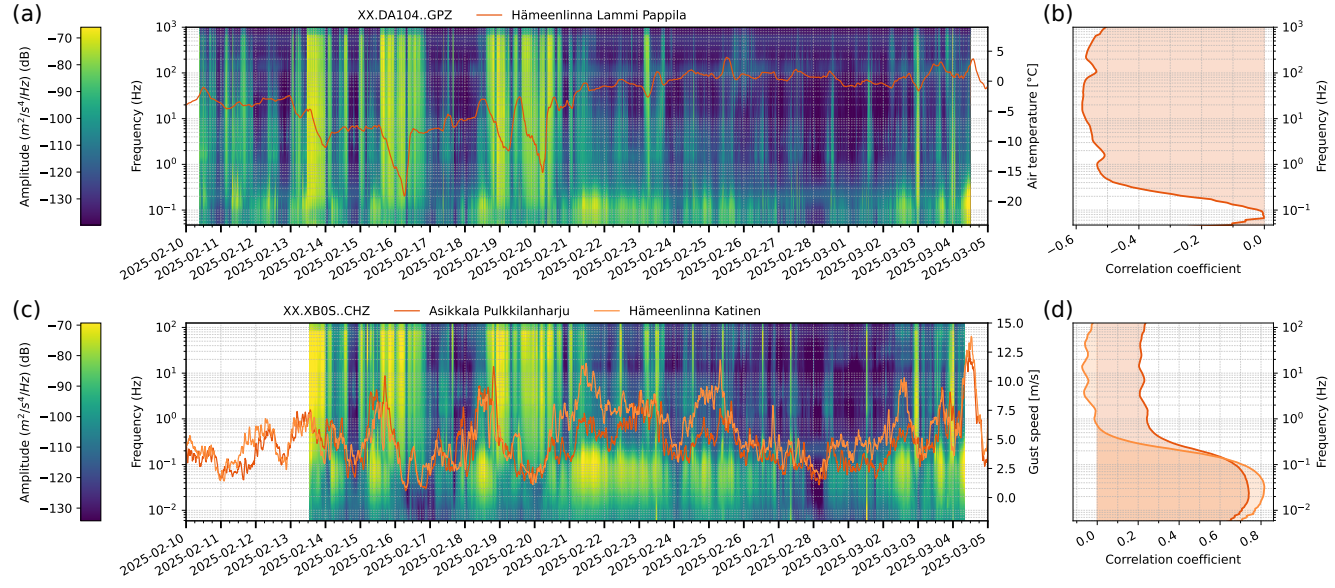

Figure 10. Comparison of seismic energy and meteorological data for February 2025. (a) A spectrogram of vertical component geophone data and air temperature data. (b) Frequency dependent correlation between seismic energy and air temperature. (c) A spectrogram of vertical component broadband data and wind speed data. (d) Frequency dependent correlation between seismic energy and wind speed. Spectrograms in panels (a) and (c) are obtained using 5 and 60 min windows, respectively, with 80% overlap.

https://doi.org/10.5194/egusphere-2026-2106
Preprint. Discussion started: 4 June 2026

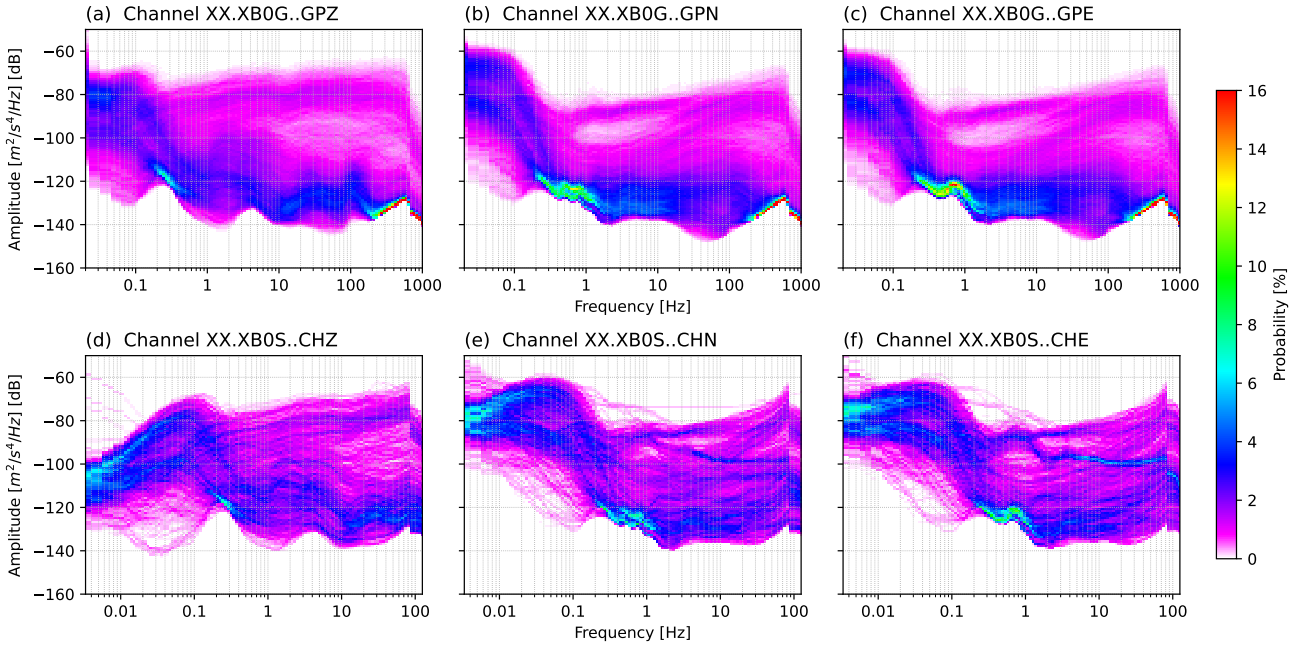

Figure 11. Probabilistic power spectral densities (PPSD). The PPSDs of (a–c) geophone and (d–f) broadband seismometer three component data are calculated from the full 20-day recording using window lengths of 300 s and 1 h, respectively. The instruments were co-located in Array B.

https://doi.org/10.5194/egusphere-2026-2106
Preprint. Discussion started: 4 June 2026

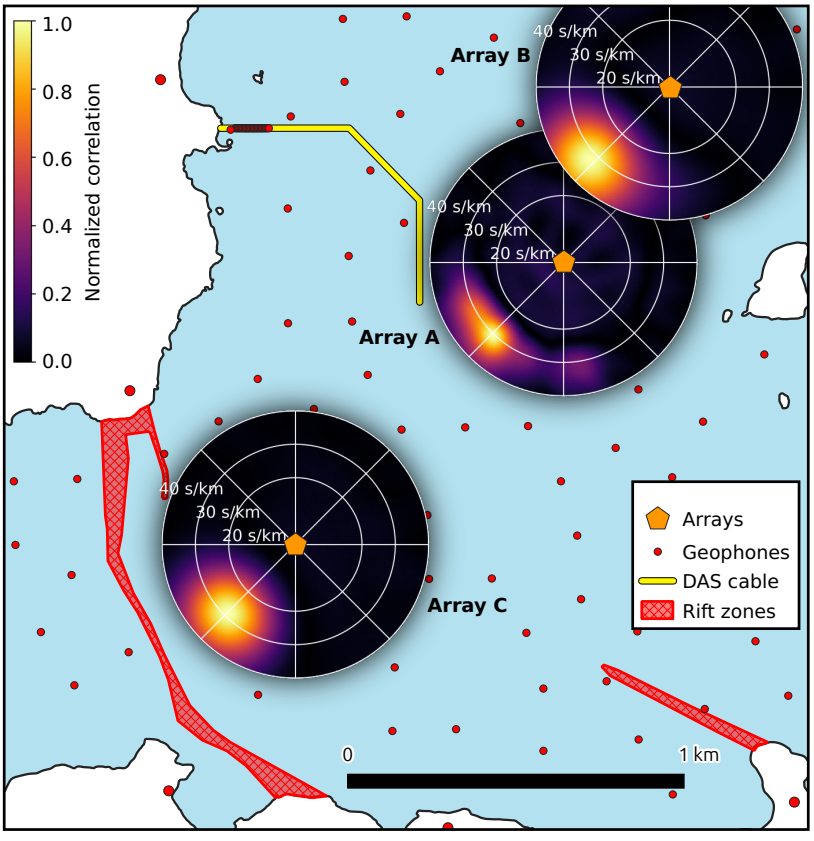

Figure 12. Cross-correlation beamforming results using vertical-component waveforms recorded by the circular arrays between 13:00 and 14:00 UTC on 15 February 2025. The orange symbols indicate the array locations on the map, and the contours of the beamformer output indicate slowness in s km^{-1}. The red areas indicate major rift zones of the lake ice.

https://doi.org/10.5194/egusphere-2026-2106
Preprint. Discussion started: 4 June 2026

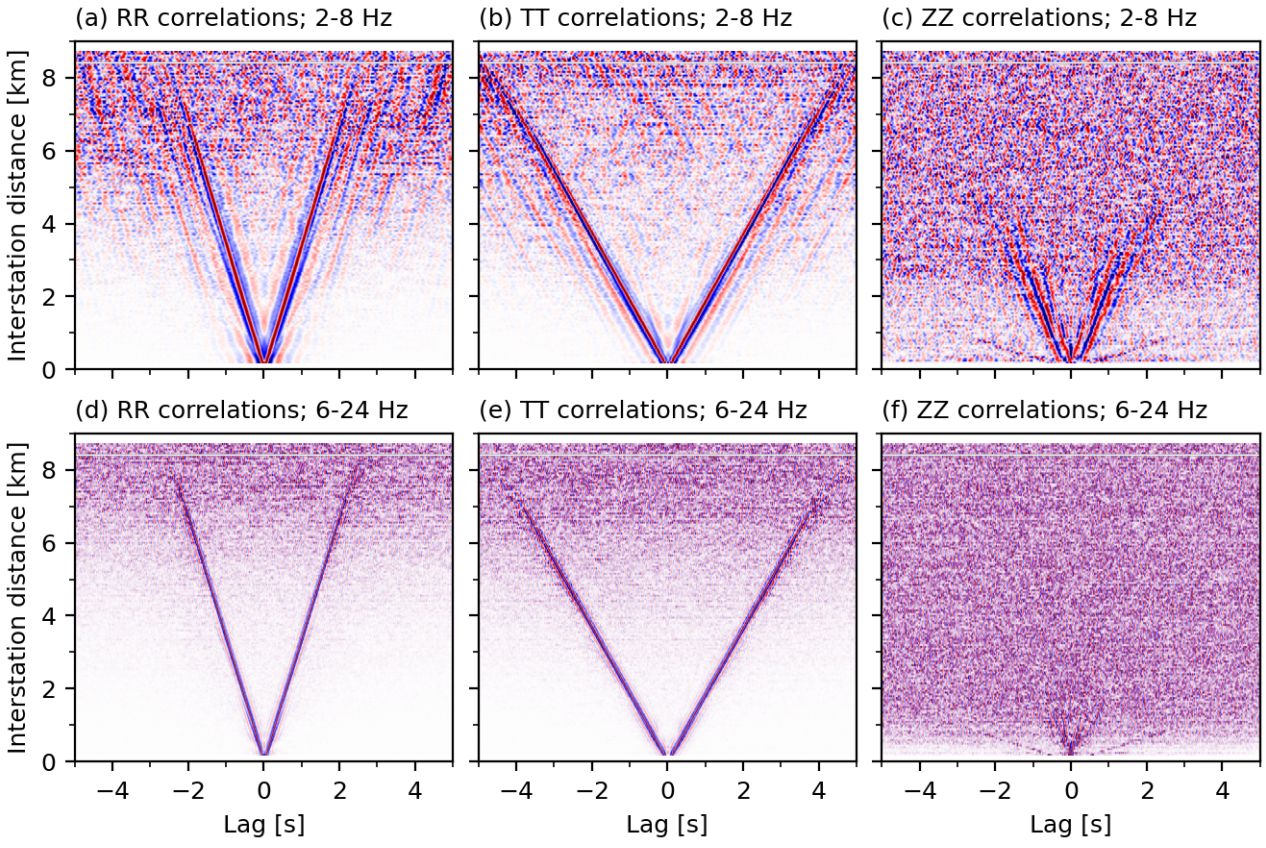

Figure 13. Ambient field correlation gathers filtered between (a–c) 2–8 Hz and (d–f) 6–24 Hz. The bin width is 50 m. Correlations are scaled by the largest amplitude in each distance bin. The estimated propagation velocities of the QS_0 mode in the radial-radial RR data, the SH_0 mode in the transverse-transverse TT data, and again of the vertical component motion of the QS_0 mode in the vertical-vertical ZZ data are 3380 m s^{-1}, 1824 m s^{-1}, and 2850 m s^{-1}, respectively. These modes are not dispersive, but the spatial coherence depends on frequency. The ZZ data resolve acoustic propagation with a velocity of 340 m s^{-1}.

https://doi.org/10.5194/egusphere-2026-2106
Preprint. Discussion started: 4 June 2026

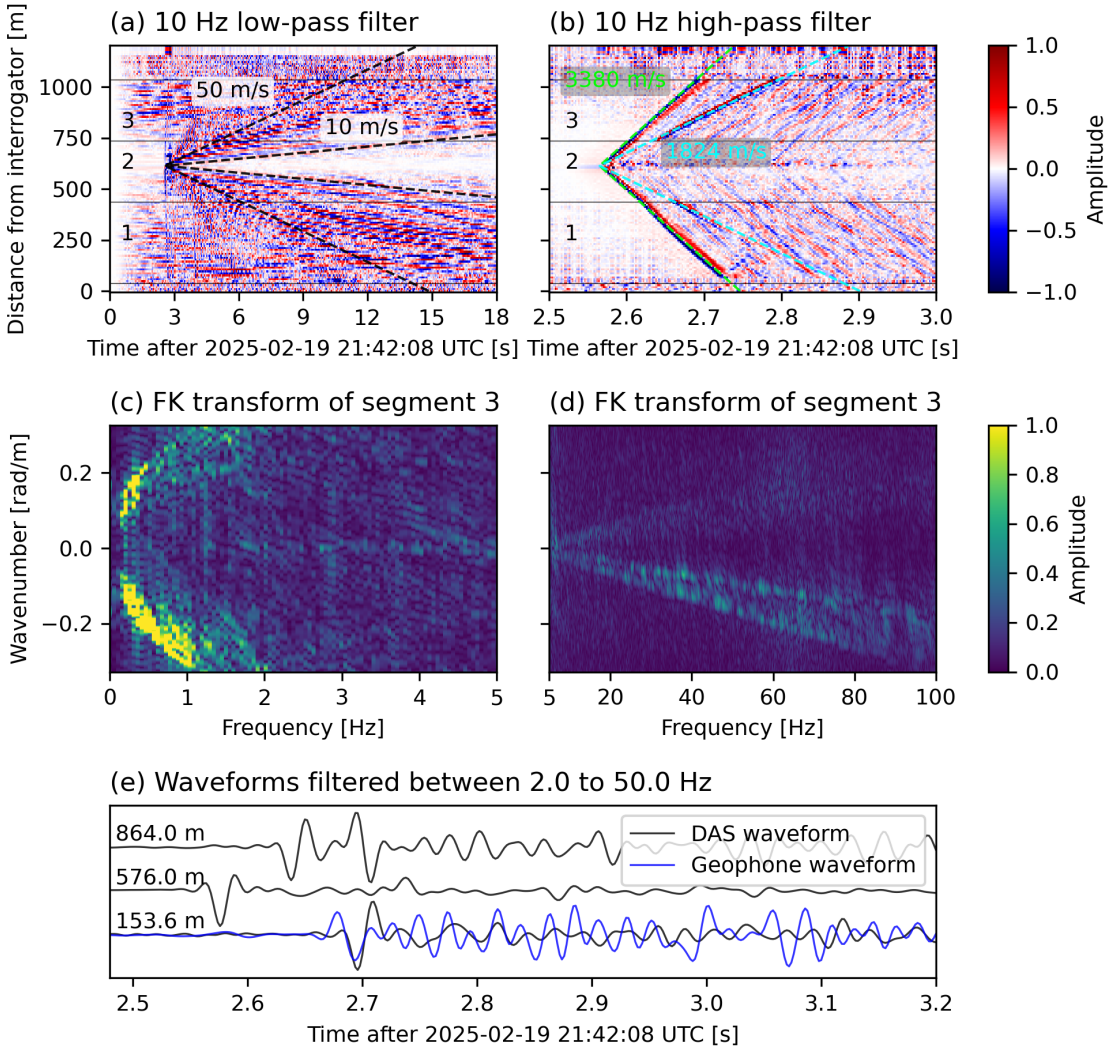

Figure 14. Data examples from the fibre optic cable. Icequake records from 21:42 UTC on 19 February 2025 at (a) low and (b) high frequencies. The horizontal black lines in panels (a) and (b) indicate the three 400 m, 300 m, and 300 m long cable segments away from the shore (Fig. 3). Black dashed lines in panel (a) indicate the minimum and maximum apparent velocity of QS waves. Green and blue dashed lines in panel (b) indicate the apparent velocity of QS_0 and SH_0 waves, respectively. Panels (c) and (d) show the FK transform obtained from data along cable segment three (736 - 1036 m). (e) DAS system observations and colocated geophone records. The waveforms are normalized by their maximum amplitude.

https://doi.org/10.5194/egusphere-2026-2106
Preprint. Discussion started: 4 June 2026

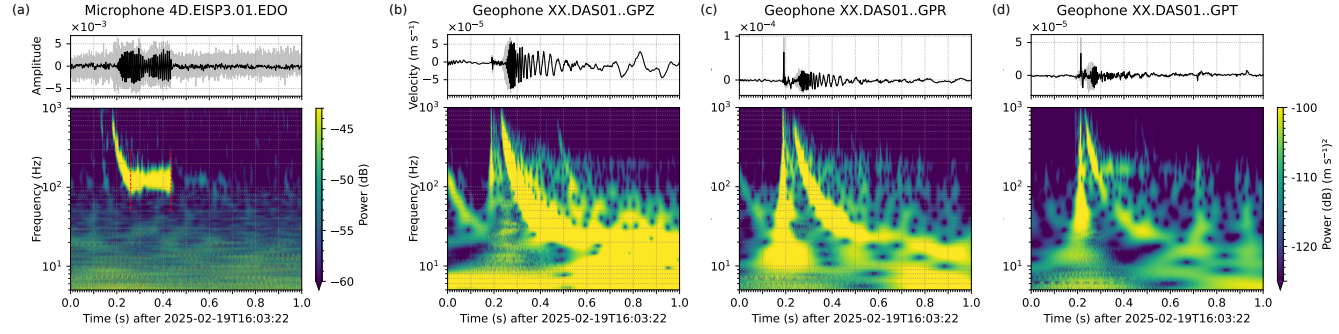

Figure 15. An example of seismo-acoustic coupling. A seismic event recorded on (a) the microphone and (b–d) a line array geophone at 15 m distance. Geophone data are rotated into the ZRT system. The geophone components show the QS_0 and QS modes on the vertical and radial component and the SH_0 and QS modes on the transversal component. The gray time series are unfiltered data and the black traces are filtered between 1 Hz and 250 Hz. The bottom panels show the corresponding wideband spectrograms. In panel (a), the wavelet spectrogram shows the dispersive QS mode until it transitions into the air-coupled wave.

https://doi.org/10.5194/egusphere-2026-2106
Preprint. Discussion started: 4 June 2026

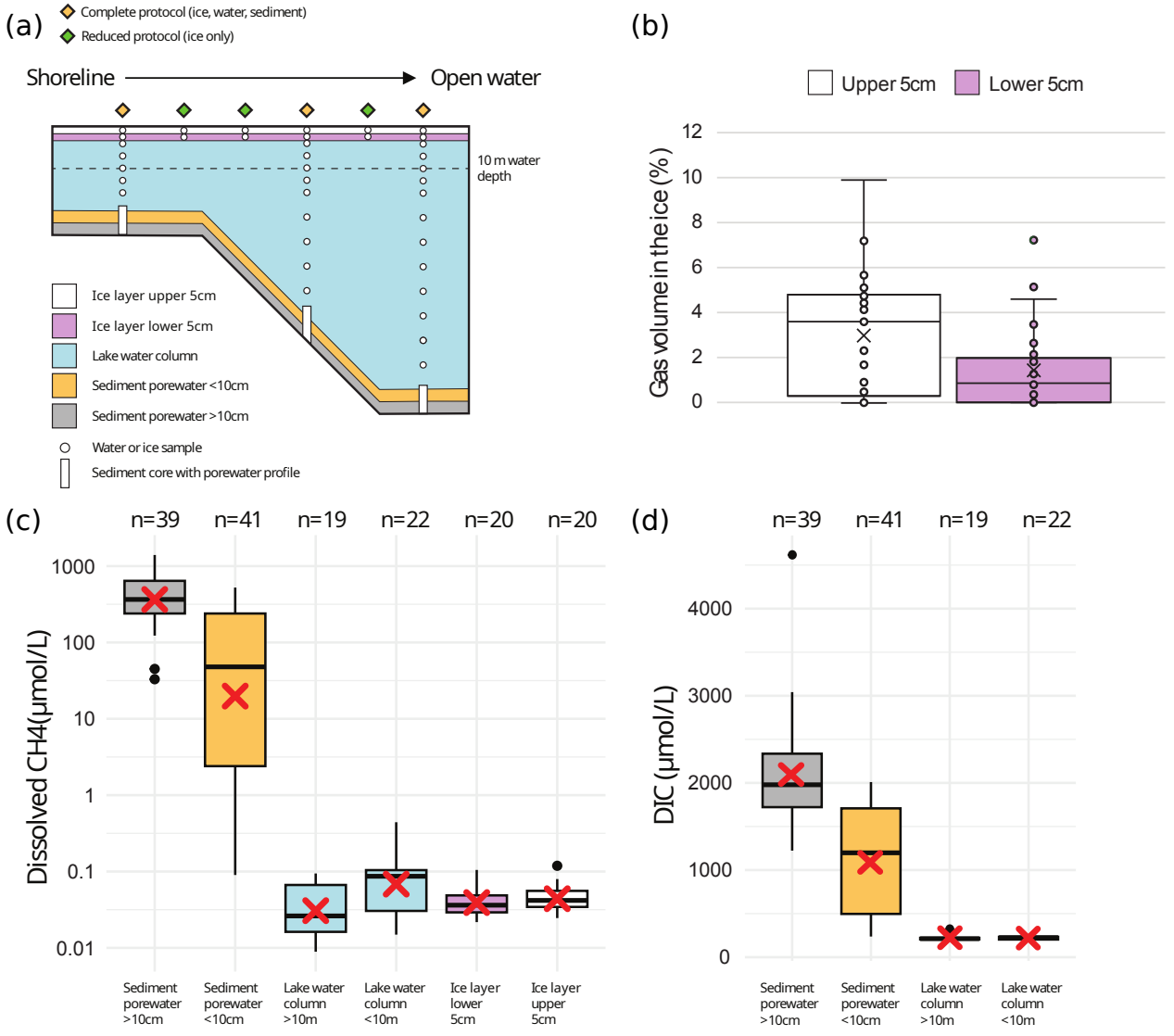

Figure 16. (a) Schematic of the sampling approach for determinations of dissolved methane (CH_4). The yellow and green symbols correspond to the high and intermediate intensity sampling protocols discussed in Figure 6. (b) Gas volume in the ice (percent of total volume) at 29 random locations sampled for the uppermost 5 cm layer and lowermost 5 cm layer. (c) Summary of all CH_4 concentration data by sample type. (d) Summary of all dissolved inorganic carbon (DIC) data by sample type. In (c) and (d), the population size n by sample type is indicated. The total number of CH_4 samples is 161. Boxes in (b), (c), and (d) show the interquartile ranges, whiskers represent the range of observed values within 1.5 times the interquartile range, and crosses represent the arithmetic mean. In (b), all data points are shown, whereas in (c) and (d) only points outside the whiskers are shown. Note that CH_4 at equilibrium with atmosphere is $\sim 0.005 \mu$mol/L.

https://doi.org/10.5194/egusphere-2026-2106
Preprint. Discussion started: 4 June 2026

Appendix A

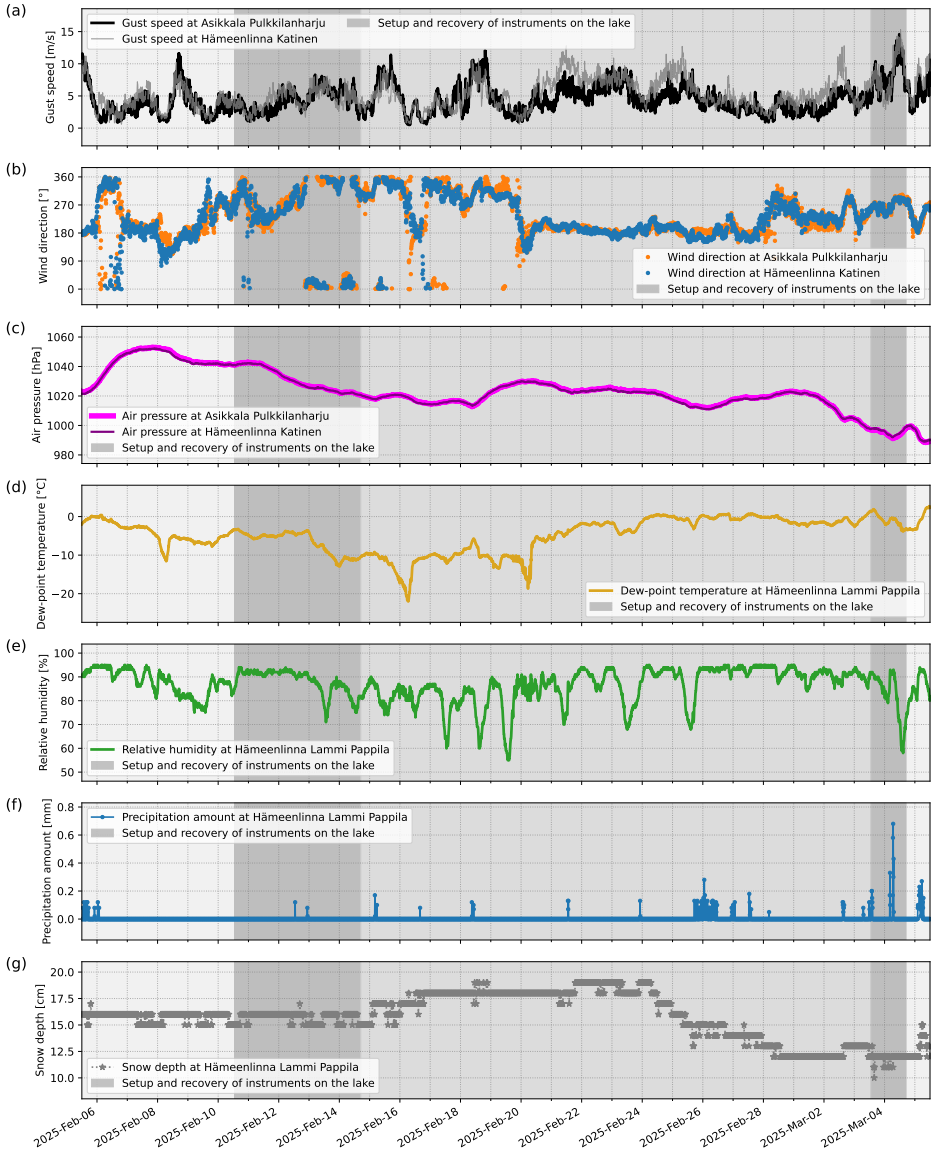

Figure A1. Meteorological observations during the on-ice deployment (Finnish Meteorological Institute, 2025). (a–b) Wind gust speed and wind directions recorded at Asikkala Pulkkilanharju and Hämeenlinna Katinen, 30 and 35 km from Lake Pääjärvi, respectively. (c) Air pressure, (d) dew point, (e) relative humidity, (f) precipitation amount and (g) snow depth recorded at Lammi Pappila at the Lammi Biological Station. Shades of gray indicate deployment phases.

https://doi.org/10.5194/egusphere-2026-2106
Preprint. Discussion started: 4 June 2026

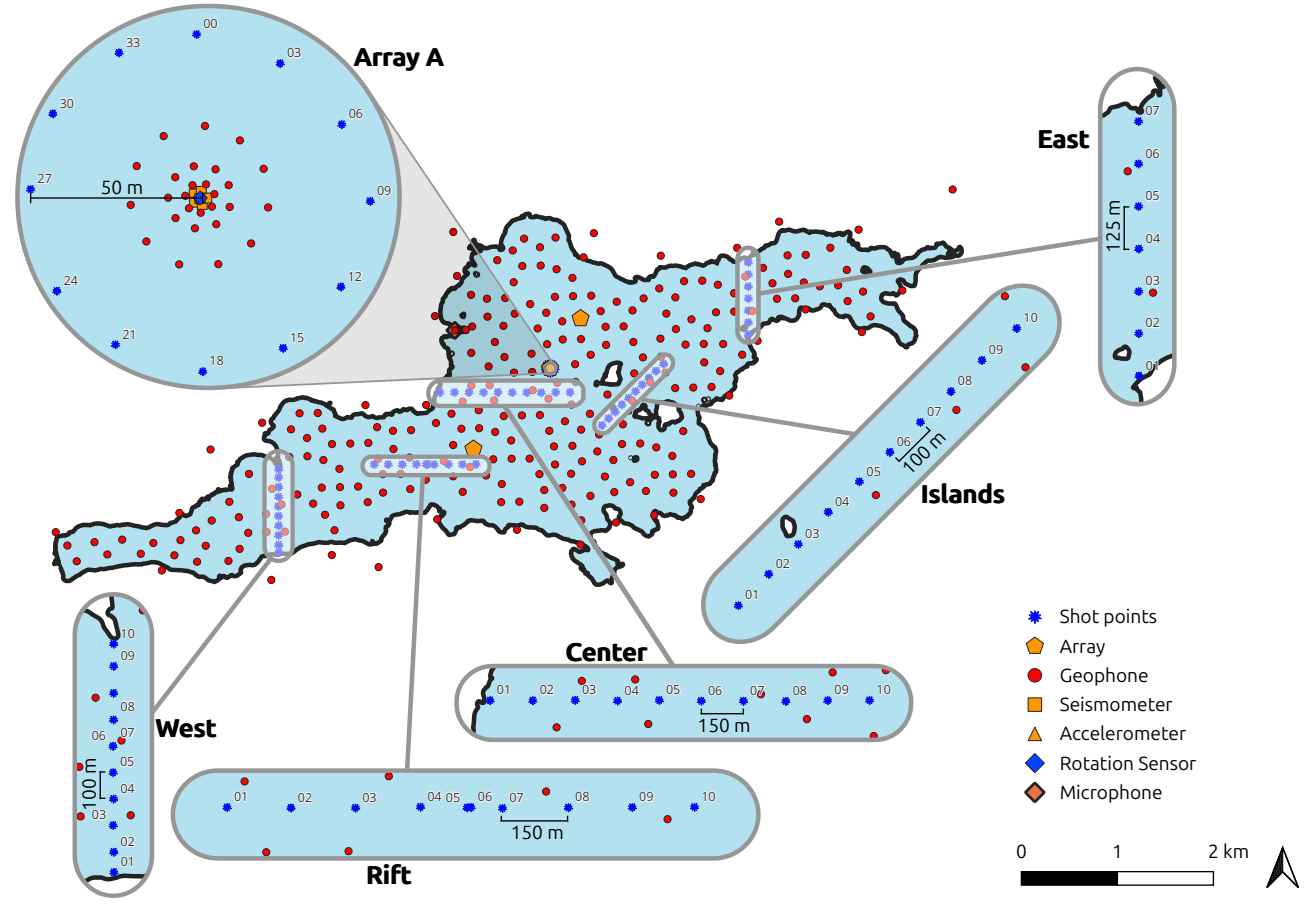

Figure A2. Hammer shots were applied at 49 locations (blue stars) along five lines and in a circle around Array A.

https://doi.org/10.5194/egusphere-2026-2106
Preprint. Discussion started: 4 June 2026

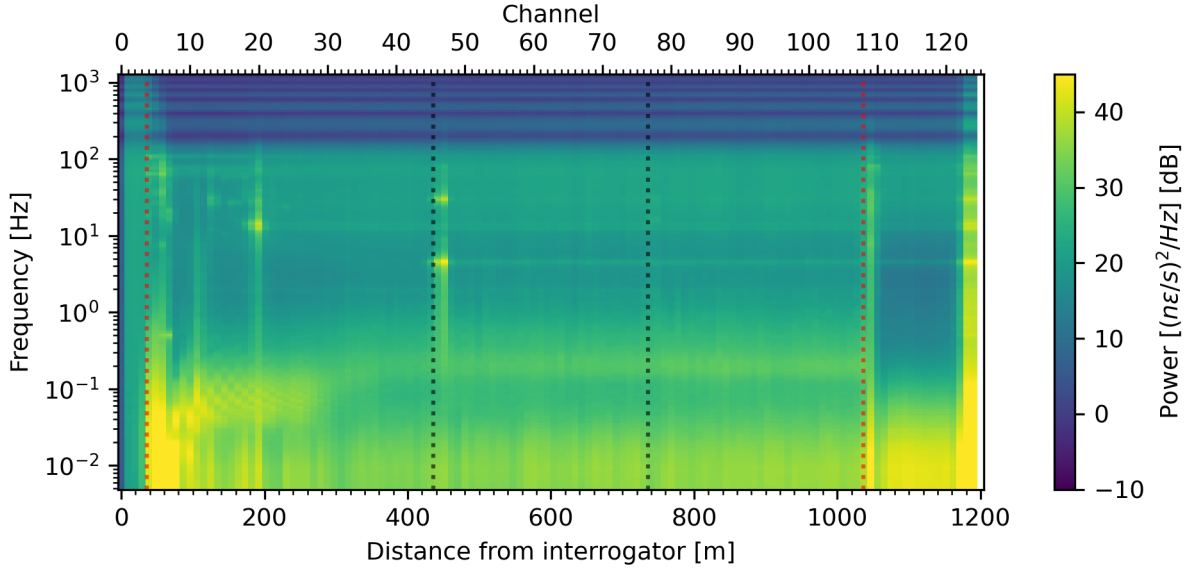

Figure A3. Spectrogram of DAS channel data recorded on 15 February 2025. Red dashed lines indicate coiled cable segments. Black dashed lines mark the cable corners.